Optimization of plasmonic metasurfaces: a homogenization-based design

Nicolas Lebbe, Kim Pham, Agnes Maurel

Preprint submitted to
Journal of Computational Physics

Optimization of plasmonic metasurfaces: a homogenization-based design

Nicolas Lebbe[a,*], Kim Pham[b], Agnès Maurel[c]

[a]*LAPLACE, Université de Toulouse, CNRS, INPT, UPS, 2 Rue Charles Camichel, 31000 Toulouse, France*
[b]*IMSIA, CNRS, EDF, CEA, ENSTA Paris, Institut Polytechnique de Paris, 828 Bd des Maréchaux, 91732 Palaiseau, France*
[c]*Institut Langevin, ESPCI Paris, Université PSL, Sorbonne Université, Université de Paris, CNRS, 1 rue Jussieu, 75005 Paris, France*

ARTICLE INFO

Keywords:
Interface homogenization
Quasi-periodic homogenization
Optimization
Finite element method

ABSTRACT

This article deals with the optimization of resonant plasmonic metasurfaces through their surface-homogenized counterpart. The derivation of effective transition conditions that takes into account the spatially varying geometries is done using locally periodic surface homogenization. The resulting model reduces the numerical cost of simulating these metasurfaces, thus allowing to find their design using adjoint-based optimization methods. This new algorithm is presented in details, together with various numerical examples to asses its validity and compare its performance with the classical design based on local phase matching.

1. Introduction

Metasurfaces are arrays of "meta-atoms" with thickness h and pattern size s much smaller than the wavelength λ_0 of the incident waves [1, 2]. Despite their modest dimensions, these metasurfaces can have very significant effects on the waves passing through them when their meta-atoms are resonant [3]. Through clever design, they have allowed wavefront manipulations to realize deflectors, lenses, holograms and cloaking devices [4, 5, 6, 7, 8, 9].

Clever design suggests that some kind of optimization has been used and in practice, optimization by means of simulating the actual metasurfaces can become prohibitively time-consuming. To avoid such brute-force optimization, one classical strategy, that will be refereed to the *local phase matching* method (LPM) afterward, consists in analyzing each meta-atom individually, with the intuitive idea that it will behave locally in the same way whatever the configuration of the array in which it is located. An alternative, as developed in applied mathematics [10], consists in replacing a whole real structure by an effective one thanks to homogenization. By nature, the effective structure is simpler to simulate and therefore the optimization process is less expensive.

The analysis of periodic metasurfaces using the homogenization theory became classical in electromagnetism [2, 11, 12, 13, 14], acoustics [15, 16], elastodynamics [17, 18] and water waves [19, 20] and it results in effective jump (or "transition") conditions of the fields instead of their usual continuity relations (see Figure 1); the transition also involve effective parameters that may be known explicitly or given by the resolution of simple elementary static

*Corresponding author:
E-mail addresses: nicolas.lebbe@laplace.univ-tlse.fr (N. Lebbe), kim.pham@ensta-paris.fr (K. Pham), agnes.maurel@espci.fr (A. Maurel)

problems. In electromagnetism, the general structure of the jumps are given by the so-called Generalized Sheet Transition Conditions (GSTCs) and the effective parameters can be casted within tensors named surface susceptibility tensors. When the meta-atoms have characteristics varying spatially along the metasurface, which is the case for practical applications, periodic homogenization has to be adapted and this has lead to *locally periodic* (a.k.a. quasi-periodic) homogenization [21, 22]. As we shall see in the present study, this results in effective jump conditions which have almost the same structure as in the periodic case but involving spatially varying susceptibility tensors.

In this paper, we present optimization and homogenization-based design of plasmonic metasurfaces (i.e. made of metallic meta-atoms sustaining local plasmonic resonances) in two dimensions and provide illustrative applications, namely deflectors and flat lenses. Our analysis partly relies on a previous study [23] in which we determined the GSTC susceptibility tensors for plasmonic metasurfaces in the periodic case. In section 2, we adapt this two-scale homogenization approach to the locally-periodic case, when the properties of the meta-atoms are allowed to vary slowly along the metasurface. Note that such homogenization has been developed fairly recently for non resonant acoustic metasurfaces [24, 22] but the resonant case, although technically not more difficult, has not be addressed. The optimization procedure, performed on the resulting homogenized metasurface, is detailed in section 3. For the sake of completeness, the classical design based on local phase matching is also recalled. Finally, illustrative examples of homogenization-based optimization on deflectors and lenses are presented in section 4, together with comparisons with local phase-based optimal designs. In the cases reported, our optimization based on homogenization proved to be significantly more efficient than optimization based on phase-matching.

2. Derivation of the quasi-periodic surface-homogenized model

Using the homogenization theory, a metasurface can be simplified into effective transition conditions using surface susceptibilities $\overline{\overline{\chi}}_{ee}$ and $\overline{\overline{\chi}}_{mm}$. In this section, we will derive the spatially-dependent values of the susceptibilities for quasi-periodic metasurfaces. The resulting transition conditions are summarized in section 2.7 and will be exploited in sections 3 and 4 to quickly obtain the response of different metasurfaces subject to incident plane waves.

2.1. Modelization of a plasmonic metasurface

We consider metasurfaces that consist of an array of cells containing arbitrary-shaped metallic meta-atoms whose properties (geometrical and/or material) are varying along the array and which is entirely surrounded by air[1], as represented in fig. 2 (top). All meta-atoms are made of a metal whose permittivity ε is such that $\mathcal{R}e[\varepsilon] < 0$ and we define the function $\varepsilon_r(\boldsymbol{x})$ which, for any spatial position $\boldsymbol{x} = (x, y)$ associates ε inside a meta-atom and 1 otherwise. We consider electromagnetic waves in the Transverse Magnetic (TM) polarization, i.e. with a magnetic field $\mathbf{H} = \mathrm{H}\mathbf{u}_z$ which is solution to the Helmholtz equation:

$$-k_0^2 \mathrm{H}(\boldsymbol{x}) = \nabla \cdot \boldsymbol{C}(\boldsymbol{x}) \quad \text{and} \quad \boldsymbol{C}(\boldsymbol{x}) := \frac{1}{\varepsilon_r(\boldsymbol{x})} \nabla \mathrm{H}(\boldsymbol{x}), \tag{1}$$

where $k_0 = 2\pi/\lambda_0$ is the wavenumber and $\lambda_0 = 1$ m a normalized wavelength.

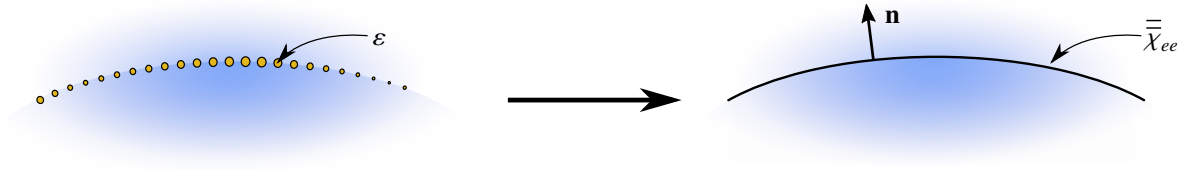

Fig. 1. Schematic representation of the effective model used for describing metasurfaces.

Since our analysis relies on an asymptotic expansion as the cell size goes to zero, we consider a sequence of metasurfaces with decreasing cell size $s_\eta = \lambda_0 \eta$ when $\eta \to 0$. To get such a sequence, we consider a smooth distribution of

[1] This choice allows us to focus on the effects of the meta-atoms rather than on the diffraction caused by the presence of different substrates.

parameters $\boldsymbol{\rho}(x)$ which is increasingly more sampled as represented in fig. 3. In this paper, without loss of generality, we will only consider circular meta-atoms and the (scalar) distribution $\rho(x)$ will refer to one geometrical parameter: the radius (relative to the cell size s_η) of the meta-atom at position x. The homogenization theory will be used to find the partial differential equation (PDE) and transition conditions verified by the field H as η goes to zero.

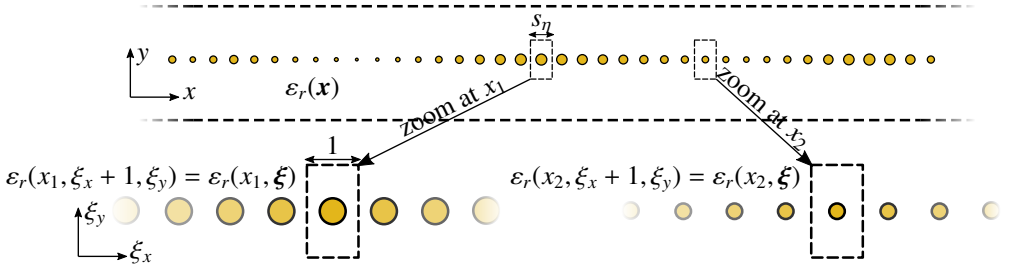

Fig. 2. Geometry of the metasurfaces considered in this paper. (top) A metasurface made of circular meta-atoms with slowly-varying radius surrounded by air. (bottom) At the microscopic level (fixed macroscopic coordinate x), the permittivity is locally periodic.

2.2. *The near- and far- fields and their matching*

To find the surface homogenized model, we will rely on a two-scale asymptotic expansion in which both the near and far fields are expanded in series of η with the introduction of a microscopic variable $\boldsymbol{\xi} = (\xi_x, \xi_y) = \boldsymbol{x}/\eta$:

$$\text{“near-field”} \quad \mathrm{A}(\boldsymbol{x}) = \sum_{n\geq 0} \eta^n \mathrm{a}^n(x, \boldsymbol{\xi}) \quad \text{near the metasurface,} \tag{2}$$

$$\text{“far-field”} \quad \mathrm{A}(\boldsymbol{x}) = \sum_{n\geq 0} \eta^n \mathrm{A}^n(\boldsymbol{x}) \quad \text{otherwise,} \tag{3}$$

where A (resp. a) represent either $\boldsymbol{C}$ or H (resp. $\boldsymbol{c}$ or h) and for all n, a^n is assumed to be periodic w.r.t. ξ_x with period 1. In order to link the far fields values above and below the metasurface, we will use the following matching conditions [13]:

$$\mathrm{A}^0(x, \pm 0) = \lim_{\ell \to +\infty} \mathrm{a}^0(x, \xi_x, \pm\ell), \tag{4}$$

$$\mathrm{A}^1(x, \pm 0) = \lim_{\ell \to +\infty} \mathrm{a}^1(x, \xi_x, \pm\ell) \mp \ell \partial_y \mathrm{A}^0(x, \pm 0). \tag{5}$$

These conditions connect the far-fields values at $y = \pm 0$ to the near-fields values at infinity ($\xi_y = \pm\infty$). Note that these relations also already tell us that A^0 and A^1 do not depend on ξ_x at $\xi_y = \pm\infty$.

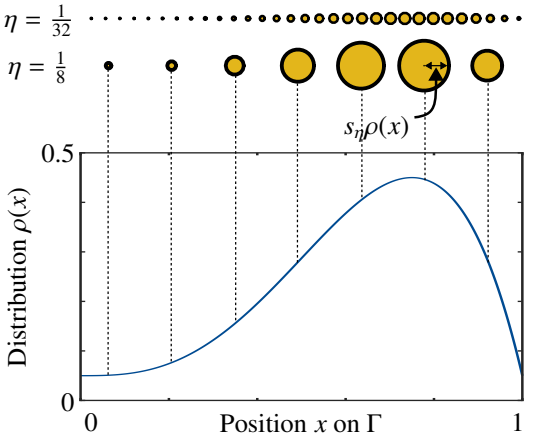

Fig. 3. Schematic definition of the sequence of metasurfaces considered during the homogenization process for an arbitrary distribution $\rho(x)$ on an interface $\Gamma = (0, 1)$.

To take into account the quasi-periodicity of ε_r, we consider a model of the permittivity which varies at the microscopic scale (as in the periodic homogenization) and macroscopically with x to account for the *slow* change from cell to cell. More precisely, we replace $\varepsilon_r(\boldsymbol{x})$ with $\varepsilon_r(x, \boldsymbol{\xi})$ such that for all $(x, \boldsymbol{\xi})$:

$$\varepsilon_r(x, \boldsymbol{\xi}) = \begin{cases} \varepsilon & \text{if } \boldsymbol{\xi} \in \Omega(x), \\ 1 & \text{otherwise.} \end{cases}$$

where $\mathcal{D} = (-1/2, 1/2) \times \mathbb{R}$ is the unit cell and the region of the meta-atom is $\Omega(x) \subset \mathcal{D}$ at position x. The definition of $\Omega(x)$ is given by the distribution of parameters. For circular meta-atoms, we have $\Omega(x) = D(\boldsymbol{0}, \rho(x))$ where $D(\boldsymbol{x}, r)$ is the disk centered at $\boldsymbol{x}$ of radius r. According to the assumption of locally periodic arrangement, we consider ξ_x-periodic condition (at each x value) as represented in fig. 2 (bottom), namely

$$\varepsilon_r(x, \xi_x + 1, \xi_y) = \varepsilon_r(x, \xi_x, \xi_y).$$

2.3. *Equations verified by the near and far fields*

By injecting the far fields expansions of eq. (3) into eq. (1) and separating each power of η, we find that for all index $n \geq 0$ and $\boldsymbol{x}$ such that $y \neq 0$:

$$-k_0^2 \mathrm{H}^n = \nabla_{\boldsymbol{x}} \cdot \boldsymbol{C}^n \quad \text{and} \quad \boldsymbol{C}^n = \nabla_{\boldsymbol{x}} \mathrm{H}^n, \tag{6}$$

where the differential operator is written as $\nabla = \nabla_{\boldsymbol{x}}$. Expectedly, far from the metasurface, the field follows the Helmholtz equation in free space. To fully describe the far fields, we need to connect the values above and below the effective interface $\Gamma = \{\boldsymbol{x}, y = 0\}$ using the matching conditions of eqs. (4) and (5) and the values of the near fields at infinity.

Thanks to the dependency of the different near fields $\mathrm{a} = \mathrm{h}, \boldsymbol{c}_x, \boldsymbol{c}_y$ on both x and $\boldsymbol{\xi}$, the differential operator writes as $\nabla_{\boldsymbol{x}} \mathrm{a} = \partial_x \mathrm{a} \mathbf{u}_x + \frac{1}{\eta} \nabla_{\boldsymbol{\xi}} \mathrm{a}$. Injecting the near field expansions of eq. (2) up to the first order into eq. (1) and separating the terms in front of η^{-1} and η^0 (note that the first order truncation results in missing terms at the order η^1 but this power of η is not considered hereafter) lead to the following equations in $\mathcal{D}$:

$$0 = \nabla_{\boldsymbol{\xi}} \cdot \boldsymbol{c}^0, \tag{7}$$

$$-k_0^2 \mathrm{h}^0 = \partial_x \boldsymbol{c}_x^0 + \nabla_{\boldsymbol{\xi}} \cdot \boldsymbol{c}^1, \tag{8}$$

$$\mathbf{0} = \nabla_{\boldsymbol{\xi}} \mathrm{h}^0, \tag{9}$$

$$\boldsymbol{c}^0 = \frac{1}{\varepsilon_r} \left(\partial_x \mathrm{h}^0 \mathbf{u}_x + \nabla_{\boldsymbol{\xi}} \mathrm{h}^1 \right). \tag{10}$$

These equations describe the near field propagation up to the first order.

2.4. *Jump conditions at the order 0*

From eq. (9), we can deduce that the zero-th order near field h^0 does not depends on $\boldsymbol{\xi}$. The matching condition of eq. (4) then gives $\mathrm{h}^0(x, \boldsymbol{\xi}) = \mathrm{H}^0(x, 0)$ for all $\boldsymbol{\xi}$ and therefore that

$$\mathrm{H}^0(x, +0) - \mathrm{H}^0(x, -0) = 0. \tag{11}$$

To find the jump condition on $\boldsymbol{C}_y^0$, as we shall work with diverging integrals, we define

$$\mathcal{D}_\ell = (-1/2, 1/2) \times (-\ell, \ell),$$

with $\ell > 0$ large enough so that $\Omega(x) \subset \mathcal{D}_\ell$ (and $\mathcal{D}_\ell \to \mathcal{D}$ for $\ell \to +\infty$). Integrating eq. (7) over $\mathcal{D}_\ell$ and passing to the limit when $\ell \to +\infty$ in eq. (4) provides

$$\boldsymbol{C}_y^0(x, +0) - \boldsymbol{C}_y^0(x, -0) = 0. \tag{12}$$

Note that contrary to h^0, $\boldsymbol{c}_y^0$ is not constant in $\mathcal{D}$ as it depends on h^1 according to eq. (10).

2.5. *The elementary solutions and the jump conditions at order 1*

To find the jump conditions at order 1, we start by injecting eq. (10) into eq. (7) and use eq. (4) with $A = \boldsymbol{C}, a = \boldsymbol{c}$ to get that:

$$\begin{cases} \nabla_{\boldsymbol{\xi}} \cdot \left[\dfrac{1}{\varepsilon_r(x, \boldsymbol{\xi})} \left(\partial_x \mathrm{H}^0(x, 0) \mathbf{u}_x + \nabla_{\boldsymbol{\xi}} \mathrm{h}^1(x, \boldsymbol{\xi}) \right) \right] = 0 & \text{in} \quad \mathcal{D} \\ \lim\limits_{\xi_y \to \pm\infty} \partial_{\xi_y} \mathrm{h}^1(x, \boldsymbol{\xi}) = \boldsymbol{C}_y^0(x, 0) \end{cases}, \tag{13}$$

given that $\varepsilon_r = 1$ at $\xi_y = \pm\infty$ and using eqs. (11) and (12). Equation (13) show that h^1 depend linearly on both $\partial_x \mathrm{H}^0(x, 0)$ and $\boldsymbol{C}_y^0(x, 0)$, hence $(\mathrm{h}^1, \boldsymbol{c}^0)$ can be decomposed as

$$\mathrm{h}^1(x, \boldsymbol{\xi}) = \boldsymbol{Q}_x(x, \boldsymbol{\xi}) \partial_x \mathrm{H}^0(x, 0) + (\boldsymbol{Q}_y(x, \boldsymbol{\xi}) + \xi_y) \boldsymbol{C}_y^0(x, 0), \tag{14}$$

$$\boldsymbol{c}^0(x, \boldsymbol{\xi}) = \frac{1}{\varepsilon_r} \left[\partial_x \mathrm{H}^0(x, 0) \mathbf{u}_x + \nabla_{\boldsymbol{\xi}} \boldsymbol{Q}_x(x, \boldsymbol{\xi}) \partial_x \mathrm{H}^0(x, 0) + (\nabla_{\boldsymbol{\xi}} \boldsymbol{Q}_y(x, \boldsymbol{\xi}) + \mathbf{u}_y) \boldsymbol{C}_y^0(x, 0) \right], \tag{15}$$

where Q_ι for $\iota = x, y$ are the elementary solutions to

$$\left\{ \begin{array}{c} \nabla_\xi \cdot \left[\dfrac{1}{\varepsilon_r} \left(\nabla_\xi Q_\iota + \mathbf{u}_\iota \right) \right] = 0 \quad \text{in} \quad \mathcal{D} \\ \lim\limits_{\xi_y \to \pm\infty} \partial_{\xi_y} Q_\iota = 0 \end{array} \right. . \tag{16}$$

The elementary problems in eq. (16) provide the static response of the meta-atom to external excitations coming from each spatial direction and can be numerically solved using, for example, the finite element method[2]. From a physical point of view, the decompositions of eq. (14) explains that, at first order, the near field is approximately given by the quasi-static response of the meta-atoms. This approximation is valid for meta-atoms made of dielectrics with low optical indices or metals with negative permittivities such as the one considered in this study and for which localized surface plasmon resonances may appear.

2.6. *Values at infinity of the first order near fields*

In this section, we introduce for any function a of ξ_y (and ℓ large enough so that $\Omega(x) \subset \mathcal{D}_\ell$) the jump

$$[\![\mathrm{a}]\!]_{\xi_y = \ell} = \mathrm{a}_{|\xi_y = +\ell} - \mathrm{a}_{|\xi_y = -\ell}.$$

From the decomposition of the first order near field in eq. (14) we find that:

$$[\![\mathrm{h}^1]\!]_{\xi_y = \ell} = [\![Q_x]\!]_{\xi_y = \ell} \, \partial_x \mathrm{H}^0(x, 0) + [\![Q_y + \xi_y]\!]_{\xi_y = \ell} \, \boldsymbol{C}_y^0(x, 0) + 2\ell \boldsymbol{C}_y^0(x, 0).$$

From the matching condition of eq. (5) and taking $\ell \to +\infty$, it follows that

$$\mathrm{H}^1(x, +0) - \mathrm{H}^1(x, -0) = [\![Q_x]\!]_{\xi_y = \infty} \, \partial_x \mathrm{H}^0(x, 0) + [\![Q_y]\!]_{\xi_y = \infty} \, \boldsymbol{C}_y^0(x, 0). \tag{17}$$

To obtain a similar transition condition on Γ for $\boldsymbol{C}_y^1$, we first need to integrate eq. (8) over $\mathcal{D}_\ell$:

$$-k_0^2 \int_{\mathcal{D}_\ell} \mathrm{d}\boldsymbol{\xi} \mathrm{H}^0(x, 0) - \int_{\mathcal{D}_\ell} \partial_x \boldsymbol{c}_x^0 \, \mathrm{d}\boldsymbol{\xi} = [\![\boldsymbol{c}_y^1]\!]_{\xi_y = \ell} . \tag{18}$$

By injecting in eq. (18) the decomposition of eq. (15), it results that

$$[\![\boldsymbol{c}_y^1]\!]_{\xi_y = \ell} = -k_0^2 2\ell \mathrm{H}^0(x, 0) - (I_0 + I_1 + I_2)$$

where

$$\begin{aligned} I_0 &= \int_{\mathcal{D}_\ell} \partial_x \left(\frac{1}{\varepsilon_r} \partial_x \mathrm{H}^0(x, 0) \right) \mathrm{d}\boldsymbol{\xi} = \left[2\ell + \left(\frac{1}{\varepsilon} - 1 \right) \int_{\Omega(x)} \mathrm{d}\boldsymbol{\xi} \right] \partial_{xx} \mathrm{H}^0(x, 0), \\ I_1 &= \int_{\mathcal{D}_\ell} \partial_x \left(\frac{1}{\varepsilon_r} \partial_{\xi_x} Q_x \partial_x \mathrm{H}^0(x, 0) \right) \mathrm{d}\boldsymbol{\xi}, \\ I_2 &= \int_{\mathcal{D}_\ell} \partial_x \left(\frac{1}{\varepsilon_r} \partial_{\xi_x} Q_y \boldsymbol{C}_y^0(x, 0) \right) \mathrm{d}\boldsymbol{\xi}. \end{aligned}$$

From the matching condition of eq. (5) when $\ell \to +\infty$ it follows that:

$$\boldsymbol{C}_y^1(x, +0) - \boldsymbol{C}_y^1(x, -0) = [\![\boldsymbol{c}_y^1]\!]_{\xi_y = \infty} + 2\ell \partial_{xx} \mathrm{H}^0(x, 0) + 2\ell k_0^2 \mathrm{H}^0(x, 0),$$

and eventually

$$\boldsymbol{C}_y^1(x, +0) - \boldsymbol{C}_y^1(x, -0) = -\partial_x \left[\left(\left(\frac{1}{\varepsilon} - 1 \right) \int_{\Omega(x)} \mathrm{d}\boldsymbol{\xi} + \int_{\mathcal{D}} \frac{1}{\varepsilon_r} \partial_{\xi_x} Q_x \, \mathrm{d}\boldsymbol{\xi} \right) \partial_x \mathrm{H}^0(x, 0) \right] - \partial_x \left(\int_{\mathcal{D}} \frac{1}{\varepsilon_r} \partial_{\xi_x} Q_y \, \mathrm{d}\boldsymbol{\xi} \boldsymbol{C}_y^0(x, 0) \right). \tag{19}$$

[2]Note that an additional constraint such as $\int_{\mathcal{D}} Q_\iota \, \mathrm{d}\boldsymbol{\xi} = 0$ must be added to have well-defined elementary problems as they are described up to a constant. This is not a problem in practice since only the gradient of Q_ι will be significant in the final formulas.

2.7. Final transition condition up to the first order

The final transition conditions are obtained considering $\mathrm{H} \simeq \mathrm{H}^0 + \eta \mathrm{H}^1$ and $\boldsymbol{C} \simeq \boldsymbol{C}^0 + \eta \boldsymbol{C}^1$, that is to say a model valid up to the first order. Such fields $(\boldsymbol{C}, \mathrm{H})$ satisfies Helmholtz equation as each term does, from eq. (6). Next, gathering eqs. (11), (12), (17) and (19), we obtain transition conditions valid up to terms in $o(\eta^2)$. We give below their expression in terms of Generalized Sheet Transition Conditions (GSTC) [13, 25]

$$\llbracket \mathrm{H} \rrbracket = \chi_{ee}^{xx} \left\{ \boldsymbol{C}_y \right\} - \chi_{ee}^{xy} \partial_x \{\mathrm{H}\}, \tag{20}$$

$$\llbracket \boldsymbol{C}_y \rrbracket = \partial_x \left(\chi_{ee}^{yy} \partial_x \{\mathrm{H}\} \right) - \partial_x \left(\chi_{ee}^{yx} \left\{ \boldsymbol{C}_y \right\} \right), \tag{21}$$

where we have defined the jump and mean operators on the effective interface Γ as:

$$\llbracket \mathrm{A} \rrbracket = \mathrm{A}(x, +0) - \mathrm{A}(x, -0) \quad \text{and} \quad \{\mathrm{A}\} = \frac{\mathrm{A}(x, +0) + \mathrm{A}(x, -0)}{2}.$$

The electric surface susceptibilities are explicit; they take the form:

$$\chi_{ee}^{xx} = \eta \mathcal{B}_y(x), \quad \chi_{ee}^{xy} = -\eta \mathcal{B}_x(x), \quad \chi_{ee}^{yx} = \eta C_y(x), \quad \chi_{ee}^{yy} = \eta \left(1 - \frac{1}{\varepsilon}\right) \mathcal{S}(x) - \eta C_x(x),$$

where we have defined the geometrical parameter $\mathcal{S}(x)$ as the area of $\Omega(x)$ and the parameters $(\mathcal{B}_\iota(x), C_\iota(x))$ for $\iota = x, y$ are determined by the elementary problems $\mathcal{Q}_\iota$ (solutions to eq. (16)) and given by

$$\mathcal{B}_\iota(x) = \llbracket \mathcal{Q}_\iota \rrbracket_{\xi_y = \infty}, \quad C_\iota(x) = \int_{\mathcal{D}} \frac{1}{\varepsilon_r} \partial_{\xi_x} \mathcal{Q}_\iota \, \mathrm{d}\boldsymbol{\xi}.$$

Contrary to periodic surface homogenization, the tangential derivatives in eq. (21) contain the $\chi_{ee}^{yy}, \chi_{ee}^{yx}$ susceptibilities and thus partially accounts for local variations in the meta-atoms geometries. For symmetric meta-atoms such as the disks considered in this paper, we can show that the out-of-diagonal susceptibilities vanishes; that is $\chi_{ee}^{xy} = \chi_{ee}^{yx} = 0$.

2.8. Finite element implementation

In the periodic case where the susceptibilities are constants, the GSTCs of eqs. (20) and (21) can be solved analytically (see Appendix A for the normal incidence case). For non constant susceptibilities, the effective transition conditions can be implemented in the Finite Element Method (FEM) [13] or with modal methods [22] and used as a mean to simplify the simulation of quasi-periodic metasurfaces since the meta-atoms geometries does not need to be meshed. Such an implementation then requires the weak formulation verified by the effective field.

Since the real field H verifies $-\nabla \cdot \left(\frac{1}{\varepsilon_r} \nabla \mathrm{H}\right) - k_0^2 \mathrm{H} = 0$ in a domain $O \subset \mathbb{R}^2$, we find using an integrating by parts that for any test function ϕ,

$$\int_O \frac{1}{\varepsilon_r} \nabla \mathrm{H} \cdot \nabla \phi^* - k_0^2 \mathrm{H} \phi^* \, \mathrm{d}\boldsymbol{x} - \int_{\partial O} \frac{1}{\varepsilon_r} \partial_{\mathbf{n}} \mathrm{H} \phi^* \, \mathrm{d}\boldsymbol{x} = 0,$$

where $\mathbf{n}$ is the normal exterior to O. When considering the GSTCs, integration by parts on both parts $O \cap (\mathbb{R} \times \mathbb{R}^{\pm})$ of O around Γ shows that the effective field H verifies

$$\int_O \nabla \mathrm{H} \cdot \nabla \phi^* - k_0^2 \mathrm{H} \phi^* \, \mathrm{d}\boldsymbol{x} - \int_{\partial O} \partial_{\mathbf{n}} \mathrm{H} \phi^* \, \mathrm{d}\boldsymbol{x} + \int_\Gamma \llbracket \partial_y \mathrm{H} \phi^* \rrbracket \, \mathrm{d}x = 0,$$

where $\Gamma = \{\boldsymbol{x} \in O, y = 0\}$. On the effective interface, eqs. (20) and (21) gives that $\left\{\partial_y \mathrm{H}\right\} = \llbracket \mathrm{H} \rrbracket / \chi_{ee}^{xx}$ and $\llbracket \partial_y \mathrm{H} \rrbracket = \partial_x \left(\chi_{ee}^{yy} \partial_x \{\mathrm{H}\} \right)$ when $\chi_{ee}^{xy} = \chi_{ee}^{yx} = 0$. This allows to write the boundary integral as[3]:

$$\int_\Gamma \llbracket \partial_y \mathrm{H} \phi^* \rrbracket \, \mathrm{d}x = \int_\Gamma \left\{\partial_y \mathrm{H}\right\} \llbracket \phi^* \rrbracket + \llbracket \partial_y \mathrm{H} \rrbracket \{\phi^*\} \, \mathrm{d}x = \int_\Gamma \frac{1}{\chi_{ee}^{xx}} \llbracket \mathrm{H} \rrbracket \llbracket \phi^* \rrbracket - \chi_{ee}^{yy} \partial_x \{\mathrm{H}\} \partial_x \{\phi^*\} \, \mathrm{d}x.$$

[3] Note that the terms on $\partial\Gamma$ coming from the integration by part on Γ are ignored as they are equal to zero when considering an infinite or macro-periodic metasurface as in section 4

The other boundary integrals on $\partial\mathcal{O}$ depend on the considered problem and will be detailed in sections 4.1.1 and 4.2.1. It should be noted that GSTCs involve a discontinuity of the field on Γ and thus require the use of different degrees of freedom for values of H above and below Γ.

3. Design of plasmonic metasurfaces

In this section, we will present two methods which can be used to design a metasurface made of circular plasmonic meta-atoms[4]. We first precisely define in section 3.1 the type of metasurfaces that will be considered in the remainder of this article. We then present in section 3.2 the standard heuristic method used to design such metasurfaces which consists in matching the local phase induced by the meta-atoms with the desired phase changes. Finally in section 3.3 we introduce a new method which may improve the heuristic design through simulations of the whole metasurface, something that is made possible using the effective transition conditions that were determined in section 2. The next section 4 will then present examples using this second approach and compare the resulting designs to those of the method based on local phase changes.

3.1. Definition of the metasurfaces that we want to design

The goal of a metasurface is to control the transmitted and reflected waves on its surface. Without loss of generality, we will only consider in this article the case of metasurfaces acting in reflection (this choice is justified in Appendix A and Appendix B), placed at a distance $d = 0.45\lambda_0$ from a perfect electric conductor (PEC) as represented in fig. 4 and working at the normalized wavelength $\lambda_0 = 1\,\mathrm{m}$. The meta-atoms will all be metallic disks made from an artificial material of permittivity $\varepsilon = -1.05 - 0.001i$[5] and varying relative radius between $r_{\min} = 0.05$ and $r_{\max} = 0.2$ inside cells of size $s_\eta = \lambda_0\eta$ with $\eta = 1/20$. The effective interface that replaces the metasurface will be denoted by $\Gamma = \{\boldsymbol{x}, y = 0\}$. The distribution of radius on Γ will be given by the function $x \mapsto \rho(x) \in (r_{\min}, r_{\max})$. Note that for a real metasurface, we may also consider a distribution $\rho(x)$ which will then be constant inside segments of size s_η.

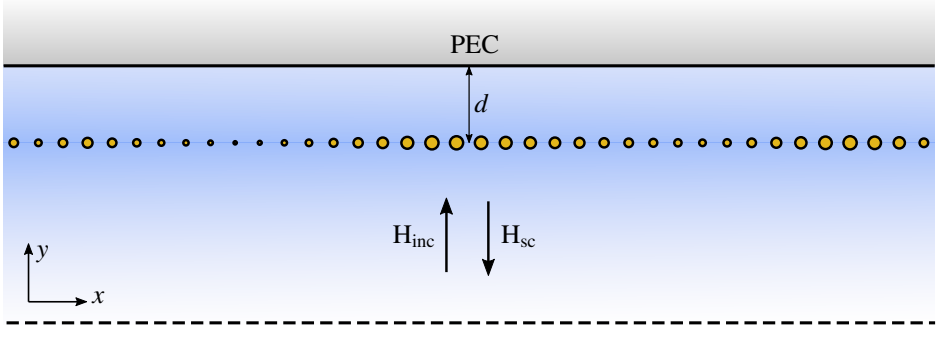

Fig. 4. Schematic representation of the plasmonic metasurfaces working in reflection that we want to design in this study.

As we will only consider normal incident plane waves, the field H below the metasurface can be expanded as

$$\mathrm{H} = \mathrm{H}_{\mathrm{inc}} + \mathrm{H}_{\mathrm{sc}} \quad \text{with} \quad \mathrm{H}_{\mathrm{inc}}(x, y) = e^{-ik_0(y-y_0)} \tag{22}$$

where $\mathrm{H}_{\mathrm{inc}}$ is the fixed incident field, H_{sc} the scattered (a.k.a. reflected) part of H and $\Gamma_0 = \{\boldsymbol{x}, y = y_0\}$ an arbitrary plane below the metasurface. Our goal is to design the metasurface, i.e., to choose the radius $\rho(x)$ of each meta-atom that composes the metasurface in order to obtain a desired reflected field $\mathrm{H}^\star_{\mathrm{sc}}$.

3.2. Heuristic design based on local phase changes

The design method that we will present here is based on two features: on one hand, in section 3.2.1, a heuristic allowing to locally link the reflected field at x to $\rho(x)$ and, on the other hand, in section 3.2.2, a matching of the reflected phase with the desired one. The whole procedure will be called the Local Phase Matching (LPM) method, and the resulting design referred to the "LP-based" one.

[4] These methods can be readily extended to any other geometric parameterization of the meta-atoms.

[5] It should be noted that for classical metals like gold and silver in the visible range, the permittivity is given by a Drude model and the absorption $-\mathcal{I}m[\varepsilon]$ is higher than the one used here, see [23].

3.2.1. Field calculation on a unit cell

To simplify the calculation of H_{sc} for any distribution $\rho(x)$, one classical heuristic is to consider that the field reflected by a meta-atom does not depend on the different radius of its neighbors. In other words, that $\mathrm{H}_{\mathrm{sc}}(x, y)$ can be obtained by simulating the unit cell at position x while considering that it is placed in a periodic metasurface, i.e. using periodic boundary conditions.

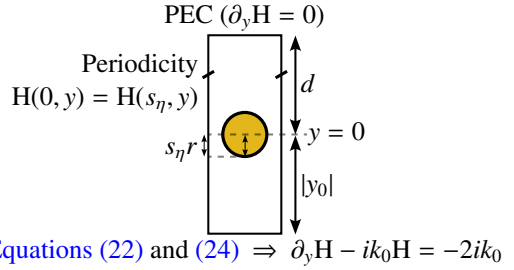

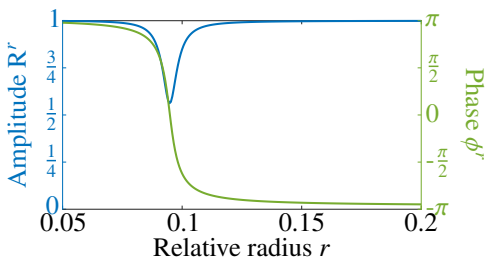

Fig. 5. (left) Boundary conditions for the simulation of a circular meta-atom with relative radius r inside a periodic metasurface of period s_η as considered in section 3.1. First-order scattering boundary condition (SBC) are used on the injection plane Γ_0. (right) Amplitude and phase of the reflection coefficient obtained by solving the Helmholtz equation in the periodic domain with varying meta-atom radius.

We denote by $\mathrm{H}^r_{\mathrm{sc}}(x, y)$ the field scattered by a periodic metasurface of circular particles with radius r when a normal incident plane wave is considered. Since the period s_η of a cell is much smaller than the wavelength, the reflected field follows Snell's law and the field $\mathrm{H}^r_{\mathrm{sc}}$ is an (outgoing) plane wave in the normal direction. As such, sufficiently far from the metasurface, the evanescent fields are essentially equal to zero and we have $\mathrm{H}^r_{\mathrm{sc}}(x, y) = \mathrm{H}^r_{\mathrm{sc}}(y)$. We then considers that at $y_0 \ll 0$:

$$\mathrm{H}_{\mathrm{sc}}(x, y_0) = \mathrm{H}^{\rho(x)}_{\mathrm{sc}}(y_0). \tag{23}$$

The values of (R^r, ϕ^r) for different radius r have been computed in fig. 5 (right) where

$$\mathrm{H}^r_{\mathrm{sc}}(y_0) = R^r e^{-i\phi^r}. \tag{24}$$

3.2.2. Local phase matching method

According to eqs. (23) and (24), the scattered field H_{sc} is equal to the desired one $\mathrm{H}^\star_{\mathrm{sc}}$ at y_0 if $\rho(x)$ is such that

$$\mathrm{H}^\star_{\mathrm{sc}}(x, y_0) = R^{\rho(x)} e^{-i\phi^{\rho(x)}}.$$

The LPM (also called UCM in [26]) then proposes to find the distribution of radius by matching the phases of the two terms in this equality. Defining $\mathrm{H}^\star_{\mathrm{sc}}(x, y_0) = R^\star(x) e^{-i\phi^\star(x)}$, we then search for $\rho(x)$ such that $\phi^\star(x) = \phi^{\rho(x)}$.

If the function $r \mapsto \phi^r$ is bijective from $r \in (r_{\min}, r_{\max})$ into $(-\pi, \pi)$ then the design can be obtained, as illustrated in fig. 6, with:

$$(r \mapsto \phi^r)^{-1} \circ \phi^\star(x) = \rho(x).$$

Three points should be kept in mind:

- To ensure that we can always find a distribution of radius no matter what the desired reflected field is, it is necessary to have a function $r \mapsto \phi^r$ which spans all phases between $-\pi$ and π. This can be achieved by considering a set of radius around a plasmonic resonance (the choice of radius in fig. 5 is further explained in Appendix B).
- When $\mathcal{I}m[\varepsilon] = 0$, the reflection coefficient R is always equal to unity which is the ideal case for applying the LPM. In practice however, real materials always have some losses (as in fig. 5) and this method does not take them into account.
- The LPM is only valid for meta-atoms having a very weak coupling with its neighbors.

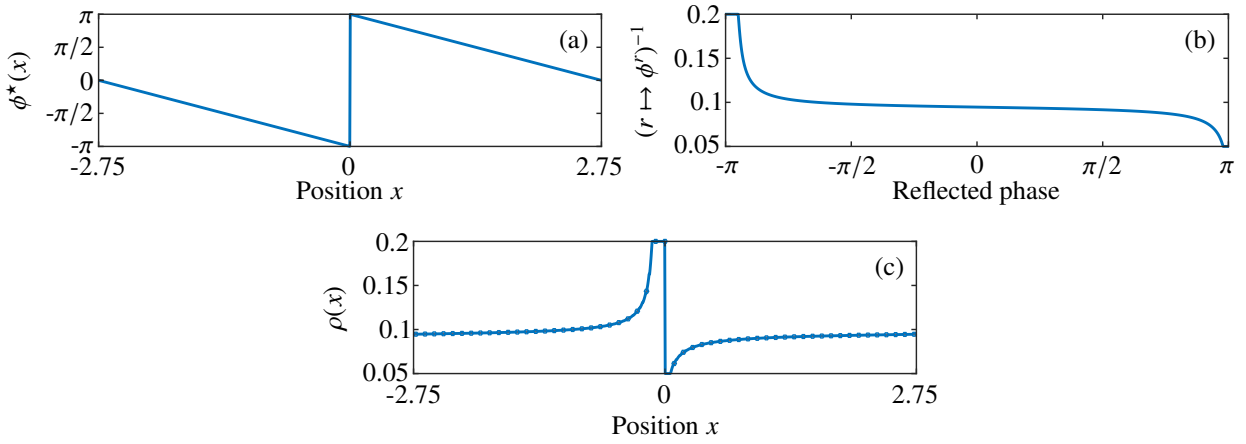

Fig. 6. Schematic representation of the LPM used to design a meta-deflector: (a) Define the expected phase $\phi^\star_{\text{sc}}(x)$ (see section 4.1.2). (b) Compute the inverse function of $r \mapsto \phi^r$ (cf. fig. 5) to find which radius is associated to which phase. (c) Find the distribution using the composition $\rho(x) = (r \mapsto \phi^r)^{-1} \circ \phi^\star(x)$. The radius of a meta-atom centered at x is then obtained by sampling the resulting graph at x.

In fig. 7 (left) we have represented the reflected field that is expected according to the LPM.

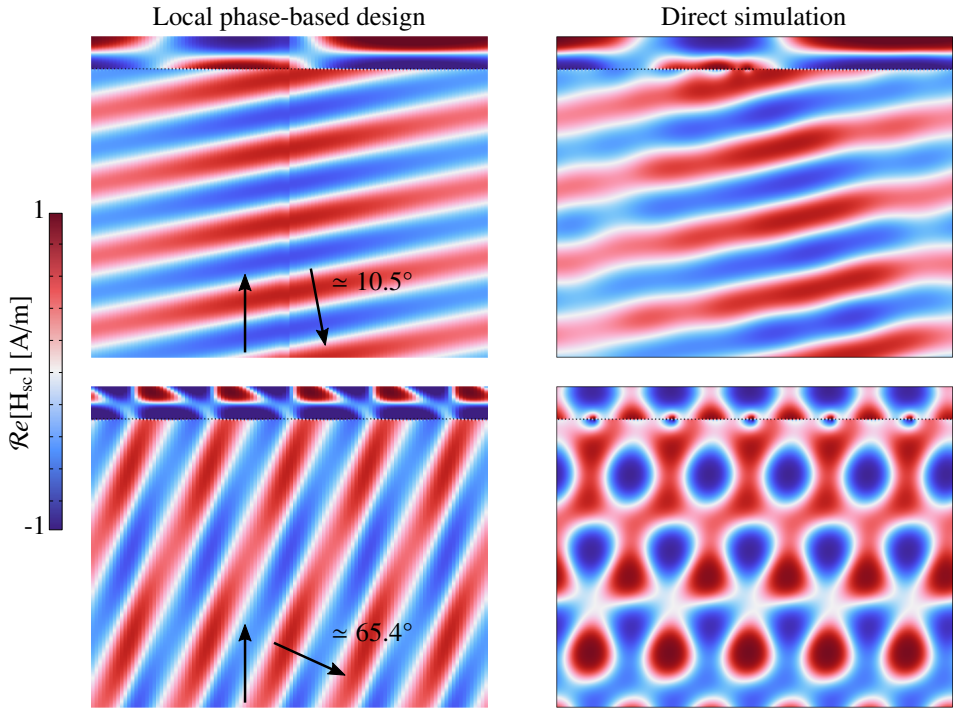

Fig. 7. (left) Design of the meta-deflector resulting from the procedure of fig. 6 and local fields calculated for each meta-atom by solving the Helmholtz equation with periodic boundary conditions as in fig. 5 (left). Note that the jump of the field in the middle of the domain comes from the fact that the function $r \mapsto \phi^r$ does not exactly cover the whole $(-\pi, \pi)$ interval and thus $(r \mapsto \phi^r)^{-1}$ is constantly extrapolated as can be seen in fig. 6 (b). (right) Direct simulation of the designed metasurface (110 meta-atoms with radius sampled from fig. 6 (c)) using the model presented in section 4.1.1.

Note that a small modification of the field is also applied to preserve the wavevector modulus. Indeed, far below the metasurface, the scattered field in each cell is assumed to be of the form $\text{H}^r_{\text{sc}}(x, y) = e^{-i(\phi^r - k_0(y-y_0))}$. In the case

of fig. 7, $\phi^\star(x) = k_0 \sin(\theta)x$ (see next section 4.1.2) meaning that:

$$\mathrm{H}_{\mathrm{sc}}(x, y) = e^{-ik_0(\sin(\theta)x-(y-y_0))},$$

which is a plane wave with a wavenumber different than k_0. That is why instead of representing $\mathrm{H}_{\mathrm{sc}}^{\rho(x)}$ in each cell, we are modifying the y component of the wavevector by showing $\tilde{\mathrm{H}}_{\mathrm{sc}}^{\rho(x)} = \mathrm{H}_{\mathrm{sc}}^{\rho(x)} e^{-ik_0(y-y_0)} e^{ik_y^{\rho(x)}}$ with $k_0^2 = |\phi^{\rho(x)}|^2 + |k_y^{\rho(x)}|^2$.

Even though this method can be really efficient as in fig. 7 (top), it fails on more difficult test cases as in fig. 7 (bottom) (higher reflection angle) and we will see that its performances can be improved with our new method.

3.3. Optimal design through numerical simulations of the effective model

We will now detail the new optimization method that we have developed and which is based on the developments of surface homogenization presented in section 2. The core of this method is similar to the one used for the optimization of mechanical structures with volume homogenization [21, 27, 28] but it has not, to the best of our knowledge, been applied to surface-homogenized resonant metasurfaces. The main steps are illustrated in fig. 8 and each of them are detailed in the following subsections.

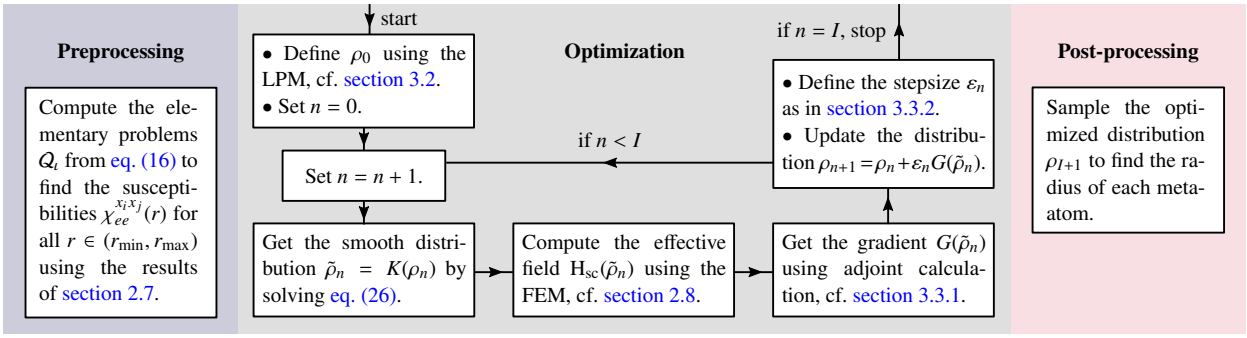

Fig. 8. Schematic steps of the homogenization-based optimization algorithm.

In order to apply any numerical optimization algorithm, one key element is the definition of a figure of merit (a.k.a. an objective function) $F(\rho)$ which describes the performance of a metasurface with radius distribution ρ and that we want to maximize. In all generality, it is possible to consider $F(\rho) = -\|\mathrm{H}_{\mathrm{sc}}(\rho) - \mathrm{H}_{\mathrm{sc}}^\star\|$, that is to minimize the difference (for a given norm) between the field $\mathrm{H}_{\mathrm{sc}}(\rho)$ associated with ρ and the expected field $\mathrm{H}_{\mathrm{sc}}^\star$. The presentation of our algorithm in this section does not depend on the definition of this function $F(\rho)$ and we will see in section 4 that more judicious figures of merit can be considered. Since $F(\rho)$ depends on the value of the field $\mathrm{H}_{\mathrm{sc}}(\rho)$, its evaluation requires numerical simulation of the metasurface. This is where the effective transition conditions GSTCs obtained in section 2 come into play as they will allow to accelerate the simulations. We will therefore consider the maximization of a functional $F(\rho)$ which involves the effective reflected field (again denoted by $\mathrm{H}_{\mathrm{sc}}(\rho)$ to simplify the notations).

In addition, it should be noted that the simulation of $\mathrm{H}_{\mathrm{sc}}(\rho)$ for any distribution ρ depends on the values of the susceptibilities for different meta-atom radius. This implies that before performing any effective simulation of a quasi-periodic metasurface, the susceptibilities associated to all possible meta-atom radius have to be computed through the simulation of the elementary problems defined in eq. (16). We will now assume that the functions $\chi_{ee}^{xx}(r)$ and $\chi_{ee}^{yy}(r)$ for any radius $r \in (r_{\min}, r_{\max})$ are known. These two susceptibilities are represented in fig. 9 with the same physical parameters as in fig. 5.

3.3.1. Sensitivity with respect to a distribution of geometrical perturbations

To find the optimal distribution $\rho : \Gamma \to (r_{\min}, r_{\max})$, we will consider a gradient-based algorithm for which it is necessary to derive the first order Taylor expansion of the figure of merit F with respect to ρ. This expansion will take the form

$$F(\rho + \epsilon\tilde{\rho}) = F(\rho) + \epsilon F(\rho)'(\tilde{\rho}) + o(\epsilon) \quad \text{where} \quad F(\rho)'(\tilde{\rho}) = \int_\Gamma G(\rho)\tilde{\rho}\,\mathrm{d}x. \tag{25}$$

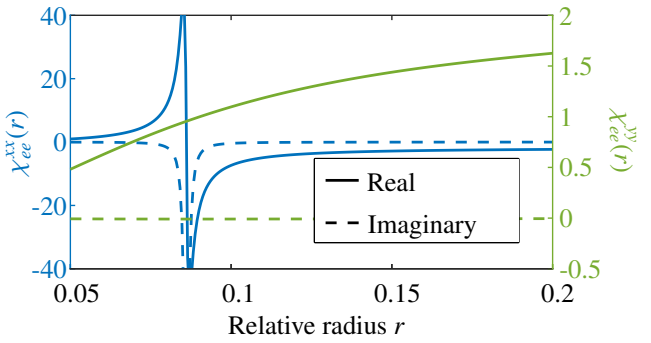

Fig. 9. Surface susceptibilities associated with the circular meta-atoms of section 3.1 obtained by solving the elementary problems of eq. (16) for different radius.

This formula will be referred to the sensitivity of $F(\rho)$ with respect to a distribution of radius perturbations $\tilde{\rho}$. Considering a sufficiently small positive value ϵ and a perturbation of the form $\tilde{\rho} = G(\rho)$ lead to $F(\rho)'(\tilde{\rho}) = \int_\Gamma |G(\rho)|^2 \, \mathrm{d}x > 0$ (when $G(\rho) \neq 0$) and thus to a new design $\rho + \epsilon\tilde{\rho}$ with better performances as $F(\rho + \epsilon\tilde{\rho}) > F(\rho)$.

Since the expression of the gradient $G(\rho)$ depends on the problem at hand, its derivation will be the treated separately in Appendix C. In general, since ρ is an infinite-dimensional vector function (or at least an element of an high-dimensional space after numerical discretization), the calculation of the gradient $G(\rho)$ is made possible by the introduction of an "adjoint" field whose solution is given by the Helmholtz equation with source terms depending on the objective function under consideration.

3.3.2. Gradient-based algorithm

Once the expression of $G(\rho)$ can be evaluated, it only remains to use it iteratively to find metasurfaces with increasingly high performances. Starting from a distribution ρ_0 such as the design obtained by the LPM of section 3.2.2, we will iteratively compute $\mathrm{H}_{\mathrm{sc}}(\rho_n)$ – the effective reflected field associated with ρ_n – and deduce a new distribution $\rho_{n+1} = \rho_n + \epsilon_n G(\rho_n)$.

Different techniques can be used to control the step ϵ_n during the gradient algorithm. In our optimization, we set ϵ_n at each iteration using $\epsilon_n = \gamma_n / \|G(\rho_n)\|_{L^\infty}$ with $\gamma_0 = 0.001$ and γ_{n+1} equal to $0.5\gamma_n$ if the new objective value is below the previous one or $1.1\gamma_n$ otherwise. This simple procedure allows to accelerate the convergence of the method by considering larger steps as long as it increases $F(\rho_n)$ but can lead to a decrease of the objective function between two consecutive iterations when the step becomes too large.

After a fixed number I of iterations, the continuous distribution of radius ρ_I is sampled at values of x spaced by a distance s_η (the size of a cell) in order to find the design of the real metasurface.

3.3.3. Discretization & regularization of the distribution

Numerically, the distribution ρ will need to be discretized. We have chosen to define it as a piecewise linear (P1) function on Γ using the same mesh as the one used in the GSTCs simulations. Since this can induce rapid variations of $\rho(x)$ on two adjacent cells, we rely on a smoothed (or "filtered") version $K(\rho)$ solution of [29, Section 3]:

$$-\nu\partial_{xx}K(\rho) + K(\rho) = \rho \quad \text{on} \quad \Gamma, \tag{26}$$

with $\nu > 0$ a small parameter equal to $(2\eta)^2$ in our examples. The borders of Γ are either terminated with periodic (for the deflectors of section 4.1) or Neumann boundary conditions (for the lenses of section 4.2). By linearity of K, the first-order expansion of $F \circ K$ is given by

$$F(K(\rho + \epsilon\tilde{\rho})) = F(K(\rho)) + \epsilon \int_\Gamma G(K(\rho))K(\tilde{\rho}) \, \mathrm{d}x + o(\epsilon).$$

A perturbation $\tilde{\rho}$ which improve the design is then given by $\tilde{\rho} = G(K(\rho))$. Indeed, replacing ρ in eq. (26) with $G(K(\rho))$, multiplying by $K(G(K(\rho)))$ and integrating by parts shows that $\int_\Gamma G(K(\rho))K(G(K(\rho))) \, \mathrm{d}x \geq 0$. In practice, this mean

that we can simply use the smoothed version $K(\rho)$ of ρ in all the calculations to always consider regular distributions during the optimization. The final design is obtained by sampling $K(\rho_I)$ instead of ρ_I.

4. Numerical examples

We will now use the two methods presented in section 3 to show the benefits of fast simulations based on the effective transition conditions obtained in section 2 to design plasmonic metasurfaces. The numerical algorithm described in section 3.3 will be applied to obtain two classes of metasurfaces, namely deflectors in section 4.1 and lenses in section 4.2, as well as more convoluted test cases showing the versatility of our approach on examples which cannot be treated with the classical method presented in section 3.2. For each example, a particular attention is paid in sections 4.1.1 and 4.2.1 to the modeling of the considered situations in order to properly simulate their behavior and to calculate the gradients required for the optimization method as explained in section 3.3.1.

4.1. Metadeflectors

The first examples of this section will consider the optimization of metadeflectors, i.e. metasurfaces reflecting an incident wave at an angle different from the one predicted by Snell's law. As we have seen in section 3.2.2 with eq. (33), a perfect deflector has to generate a reflected phase following $\phi_{\text{sc}}(x) = k_0 \sin(\theta) x$ modulo 2π, i.e. periodic with period $2\pi/(k_0 \sin(\theta)) = \lambda_0/\sin(\theta)$. We will therefore consider macro-periodic metasurfaces whose modeling is explained in section 4.1.1.

4.1.1. Modelization of a macro-periodic metasurface

Let us consider a macro-periodic metasurface of period w, i.e. for which the permittivity verifies $\varepsilon_r(\boldsymbol{x} + w\mathbf{u}_x) = \varepsilon_r(\boldsymbol{x})$. The simulation domain is then given by $O = (-w/2, w/2) \times (y_0, d)$ with d the distance between the metasurface and a perfectly reflecting surface as shown in fig. 10.

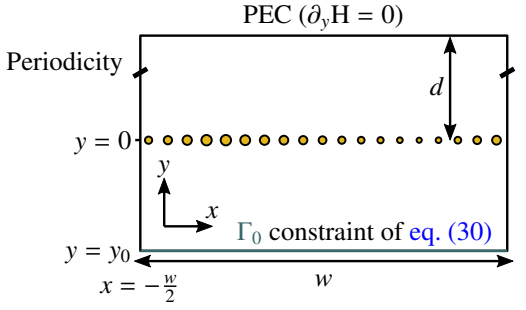

Fig. 10. Schematic representation and boundary conditions verified by the field H in the macro-periodic metasurfaces considered in section 4.1.

Since we consider waves under normal incidence, the electromagnetic excitation verifies the same periodicity w and Floquet's theorem allows us to express the field on a plane $\Gamma_0 = (-w/2, w/2) \times \{y_0\}$ as

$$\mathrm{H}(x, y_0) = \mathrm{H}_{\text{inc}}(x, y_0) + \mathrm{H}_{\text{sc}}(x, y_0) \tag{27}$$

with

$$\mathrm{H}_{\text{inc}}(x, y) = \mathrm{H}_0^{\uparrow}(x, y) \quad \text{and} \quad \mathrm{H}_{\text{sc}}(x, y) = \sum_n \mathrm{R}_n^{\mathrm{H}} \mathrm{H}_n^{\downarrow}(x, y),$$

where $\mathrm{R}_n^{\mathrm{H}}$ is the n-th order of reflection. The associated "modes" are defined as:

$$\mathrm{H}_n^{\uparrow}(x, y) := A_n e^{-i(k_{x,n}x + k_{y,n}(y - y_0))},$$
$$\mathrm{H}_n^{\downarrow}(x, y) := A_n e^{-i(k_{x,n}x - k_{y,n}(y - y_0))},$$

in which $A_n = (\omega_0 \mu_0 / (k_{y,n} w/2))^{\frac{1}{2}}$ is a normalization of the modes power and the wavevectors $\mathbf{k}_n = (k_{x,n}, k_{y,n})$ are defined by:

$$k_{x,n} := \frac{2\pi}{w} n = k_0 \sin(\theta_n) \quad \text{and} \quad k_{y,n} := \sqrt{k_0^2 - k_{x,n}^2}. \tag{28}$$

For a given macro period w, only a subset of modes - the ones such such that $|k_{x,n}| < k_0$ - are propagative and define the deflection angles achievable by the macro-periodic metasurface. The other modes are evanescent and exponentially decaying to infinity. Note that from a numerical point of view, all sums on the reflection orders are truncated to keep only the propagative modes. For an injection plane Γ_0 sufficiently far from the metasurface, the evanescent modes are close to zero and the truncation has little influence on the simulation result.

The weak formulation associated to this problem will simultaneously solve for the field H in the open domain O as well as the order of reflections $\mathbf{R}^{\mathrm{H}} = (\mathrm{R}_n^{\mathrm{H}})_n$ defining the reflected field on Γ_0. Following the presentation in section 2.8, the field H is solution for all test functions ϕ of:

$$\int_O \frac{1}{\varepsilon_r} \nabla \mathrm{H} \cdot \nabla \phi^* - k_0^2 \mathrm{H} \phi^* \, \mathrm{d}\boldsymbol{x} + \int_{\Gamma_0} \partial_y \mathrm{H} \phi^* \, \mathrm{d}x = 0,$$

where the boundary integrals are reduced to Γ_0 thanks to the PEC at $y = d$ which give that $\partial_{\mathbf{n}} \mathrm{H} = 0$ and the periodicity of the domain. Using the decomposition of eq. (27) and equivalently for the test functions that

$$\phi(x, y_0) = \sum_n \mathrm{R}_n^{\phi} \mathrm{H}_n^{\downarrow}(x, y_0), \tag{29}$$

we can write:

$$\int_{\Gamma_0} \partial_y \mathrm{H} \phi^* \, \mathrm{d}x = -i \int_{\Gamma_0} \left(k_0 A_0 - \sum_n k_{y,n} \mathrm{R}_n^{\mathrm{H}} A_n e^{-ik_{x,n}x} \right) \left(\sum_n (\mathrm{R}_n^{\phi})^* A_n e^{ik_{x,n}x} \right) \mathrm{d}x = -iwk_0 A_0^2 (\mathrm{R}_0^{\phi})^* + iw \sum_n k_{y,n} A_n^2 \mathrm{R}_n^{\mathrm{H}} (\mathrm{R}_n^{\phi})^*.$$

This is summarized by saying that H is solution for all ϕ which verifies eq. (29) of:

$$a_{\mathrm{H}}^{\varepsilon}(\mathrm{H}, \phi) + a_{\mathrm{R}}(\mathbf{R}^{\mathrm{H}}, \mathbf{R}^{\phi}) = l^0(\mathbf{R}^{\phi}) \quad \text{with the constraint} \quad \mathrm{H}(x, y_0) = \mathrm{H}_0^{\uparrow} + \sum_n \mathrm{R}_n^{\mathrm{H}} \mathrm{H}_n^{\downarrow}, \tag{30}$$

where the linear and sesquilinear forms are given by (note that the a_R and l^n forms together with the constraint on Γ_0 are similar to the one implemented in the COMSOL "periodic port" feature [30]):

$$\begin{aligned} a_{\mathrm{H}}^{\varepsilon}(\mathrm{H}, \phi) &:= \int_O \frac{1}{\varepsilon_r} \nabla \mathrm{H} \cdot \nabla \phi^* - k_0^2 \mathrm{H} \phi^* \, \mathrm{d}\boldsymbol{x}, \\ a_{\mathrm{R}}(\mathbf{R}^{\mathrm{H}}, \mathbf{R}^{\phi}) &:= iw \sum_n k_{y,n} A_n^2 \mathrm{R}_n^{\mathrm{H}} (\mathrm{R}_n^{\phi})^*, \\ l^n(\mathbf{R}^{\phi}) &:= iwk_{y,n} A_n^2 (\mathrm{R}_n^{\phi})^*. \end{aligned}$$

Equivalently, the effective field H is found to be the solution to:

$$a_{\mathrm{H}}(\mathrm{H}, \phi) + a_{\mathrm{R}}(\mathbf{R}^{\mathrm{H}}, \mathbf{R}^{\phi}) + b_{\Gamma}(\mathrm{H}, \phi) = l^0(\mathbf{R}^{\phi}) \quad \text{with the constraint} \quad \mathrm{H}(x, y_0) = \mathrm{H}_0^{\uparrow} + \sum_n \mathrm{R}_n^{\mathrm{H}} \mathrm{H}_n^{\downarrow}, \tag{31}$$

in which we have defined (note that the derivation of the b_Γ form was performed in section 2.8):

$$\begin{aligned} a_{\mathrm{H}}(\mathrm{H}, \phi) &:= \int_O \nabla \mathrm{H} \cdot \nabla \phi^* - k_0^2 \mathrm{H} \phi^* \, \mathrm{d}\boldsymbol{x}, \\ b_{\Gamma}(\mathrm{H}, \phi) &:= \int_{\Gamma} \frac{1}{\chi_{ee}^{xx}(\rho)} [\![\mathrm{H}]\!] [\![\phi^*]\!] - \chi_{ee}^{yy}(\rho) \partial_x \{\mathrm{H}\} \partial_x \{\phi^*\} \, \mathrm{d}x. \end{aligned} \tag{32}$$

Finally, note that the constraints in eqs. (30) and (31) are numerically solved thanks to the addition of a Lagrange multiplier (a periodic scalar field) on Γ_0.

4.1.2. Local phase-based design

A perfect deflector by an angle θ is defined with a scattered field given by:

$$\mathrm{H}_{\mathrm{sc}}^{\star}(x, y) = e^{-ik_0(\sin(\theta)x - \cos(\theta)(y - y_0))}.$$

The desired phase on Γ_0 must then follows

$$\phi_{\mathrm{deflector}}^{\star}(x) = k_0 \sin(\theta) x \quad \text{modulo} \quad 2\pi. \tag{33}$$

The domain being macro-periodic, only angles of the form $\theta = \theta_n := \arcsin(n\lambda_0/w)$ (see eq. (28)) are propagative and will be considered hereafter. The metasurface design can then be obtained with the LPM as illustrated in fig. 6.

Note that the expected phase given in eq. (33) can also be derived from the generalized Snell's law [3] which states that the reflection of a normal incident plane wave into an angle θ can occur if $\sin(\theta) - \sin(0) = 1/k_0 \partial_x \phi(x)$ (in the air), that is to say if $\phi(x) = k_0 \sin(\theta) x$.

4.1.3. Sensitivity of an order of reflection

In order to apply the method introduced in section 3.3, we explained that it is necessary to define an objective function that need to be maximized and to determine its sensitivity w.r.t. a perturbation of the radius distribution. Thanks to the order of reflections in eq. (27), we can define an optimal metadeflector in the angle θ_N as the metasurface with radius distribution ρ which maximizes

$$F_{\text{deflector}}(\rho) := |\mathrm{R}_N^{\mathrm{H}}|^2. \tag{34}$$

The full derivation of the gradient's expression is performed in Appendix C.1 and the result is summarized below. The gradient associated with eq. (34) is given by:

$$G_{\text{deflector}}(\rho) = \mathcal{R}e\left[\frac{(\mathrm{R}_N^{\mathrm{H}})^*}{iwk_{y,N}|A_N|^2}\left(\frac{(\chi_{ee}^{xx})'(\rho)}{(\chi_{ee}^{xx})^2(\rho)}[\![\mathrm{H}]\!][\![p]\!] + (\chi_{ee}^{yy})'(\rho)\partial_x\{\mathrm{H}\}\partial_x\{p\}\right)\right], \tag{35}$$

in which $(p, \mathbf{R}^p)$ is an "adjoint" state solution to:

$$a_{\mathrm{H}}(p, \mathring{\mathrm{H}}^*) + a_{\mathrm{R}}(\mathbf{R}^p, \mathring{\mathbf{R}}^{\mathrm{H}*}) + b_\Gamma(p, \mathring{\mathrm{H}}^*) = l^{-N}(\mathring{\mathbf{R}}^{\mathrm{H}*}).$$

Remark: Our choice of modeling allows for a physical interpretation of the adjoint state; p is the field obtained when injecting the $-N$-th mode (keep in mind that, following our definitions, the upward $-N$-th mode corresponds to the same angle as the downward N-th mode that we want to obtain). The same may not be true with different boundary conditions for wave injection and absorption. Nevertheless, an adjoint state can always be found using the same procedure as detailed in this section or by using automatic differentiation methods [31].

We will now compare the local phase-based designs of metadeflectors with the one obtained using our new method.

4.1.4. Classical deflectors

We start by optimizing metadeflectors in reflection for the order of reflection 1 to 5 using $I = 100$ iterations for our optimization method presented in section 3.3. The geometrical and physical parameters of both the metasurface and meta-atoms are given in section 3.1. The macro-period w defined in section 4.1.1 is $w = 5.5\lambda_0$. The optimization takes around 3 minutes per design and the results are summarized in fig. 11 and table 1 (note that the direct simulation of the final design takes more than half a minute compared to approximately 2 seconds for the effective simulations during the optimization).

N	1	2	3	4	5
LP-based design	0.76	0.71	0.59	0.59	0.49
H-based design	0.79	0.80	0.82	0.80	0.78
Improvement	+4%	+12%	+39%	+35%	+58%

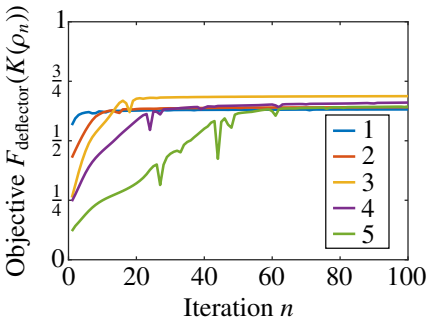

Table 1. (left) Comparison of the deflectors (values of $|\mathrm{R}_N^{\mathrm{H}}|$ *using direct simulations*) obtained using either the LPM or the optimized designs. (right) Convergence graph for the different deflectors (values of $|\mathrm{R}_N^{\mathrm{H}}|^2$ at each iteration *using the effective model*). Note that the simulations using LPM give different results than the zero-th iteration of the numerical optimization because (1) the algorithm considers the regularized distribution of section 3.3.3 and thus initially $K(\rho_0) \neq \rho_0$ (2) the convergence graph presents effective simulations while the table only shows the results of direct simulations of real metasurfaces.

We can see improvements from the initial design obtained with the LPM which is more and more important as we are taking higher orders of reflection. This is most likely due to the fact that for high diffraction orders, the LPM design varies rapidly as a function of x and thus depends strongly on local interactions between adjacent meta-atoms that are not taken into account by this method.

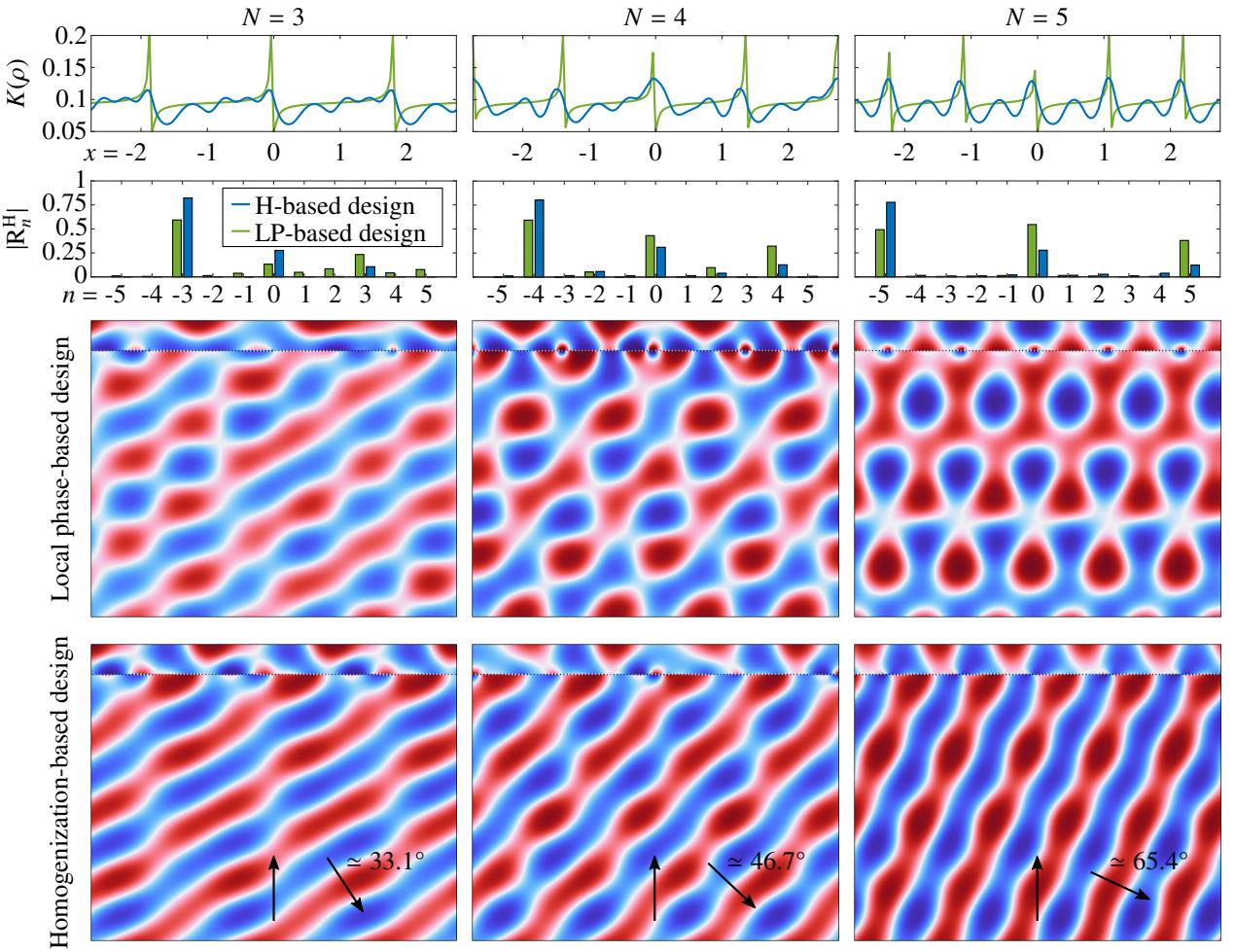

Fig. 11. LPM (third line) and optimized (fourth line) designs of the deflectors in reflection obtained with the optimization algorithm of section 3.3, deflecting a normal incident plane wave into the N-th order of reflection for $N = 3$ to 5.

4.1.5. Multiple wavelengths

In this second example, we consider the optimization of a deflector working at two different wavelengths. More precisely, we want to maximize the amplitude of two different order of reflections $\mathrm{R}_{N_1}^{\mathrm{H}_{\lambda_1}}$ and $\mathrm{R}_{N_2}^{\mathrm{H}_{\lambda_2}}$ associated with the fields $\mathrm{H}_{\lambda_\iota}$ solution to the Helmholtz equation at the wavelengths λ_ι by maximizing the objective function:

$$F_{\text{multi-deflector}}(\rho) := |\mathrm{R}_{N_1}^{\mathrm{H}_{\lambda_1}}|^2 + |\mathrm{R}_{N_2}^{\mathrm{H}_{\lambda_2}}|^2. \tag{36}$$

The LPM cannot be used here because there is not a single input and output field; we must find a compromise between the two required wavefronts. By linearity, the gradient of eq. (36) is obtained as the sum of two eq. (35). In fig. 12 we show the result of our optimization after $I = 250$ iterations starting with $\rho_0(x) = (r_{\max} + r_{\min})/2$. The same macro-periodic domain ($w = 5.5\lambda_0$) as in section 4.1.4 is considered with $\lambda_1 = \lambda_0$, $N_1 = 4$ and $\lambda_2 = 2\lambda_0, N_2 = -2$ (which corresponds to a deflection by an angle of $\theta = \pm \arcsin(|N_1|\lambda_1/w) \simeq \pm 46.7°$). Note that for simulations at λ_2 there are only 5 propagative modes while for λ_1, 11 must be accounted for.

4.2. Metalenses

The second class of metasurfaces that will be considered in this paper are metalenses, i.e. metasurfaces that reflect the incident wave by focusing it at a fixed focal point $\boldsymbol{x}_0 = (0, f_0)$ with $f_0 < 0$. Contrary to metadeflectors, these metasurfaces are not macro-periodic and therefore require a different modeling which will be the subject of section 4.2.1.

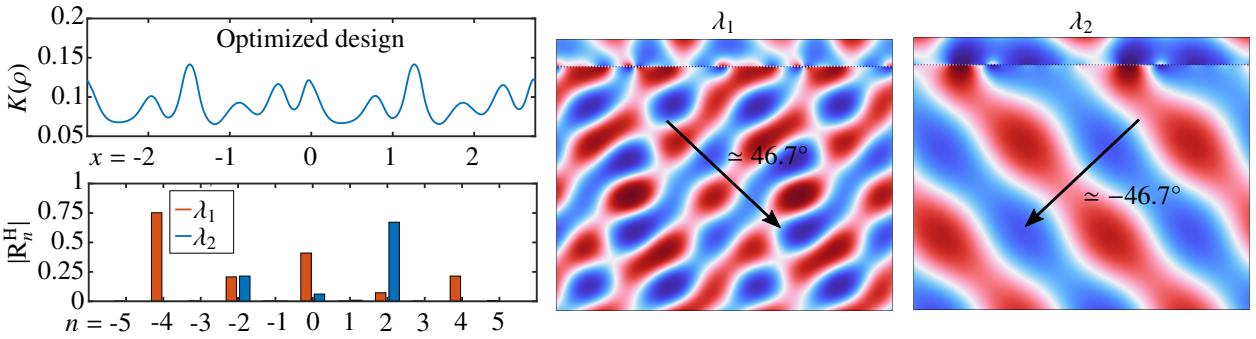

Fig. 12. Optimized metasurface in reflection which deflect a normal incident plane wave by ±46.7°depending on the wavelength.

4.2.1. Modelization of a metasurface in open space

We consider a metasurface in reflection with finite-size w. In the case of deflectors, it was possible to truncate the domain using the macro period and a decomposition of the reflected field coming from the Floquet theorem. In the case of lenses, it is necessary to consider the propagation of waves in a theoretically infinite domain. To do this, we still consider the decomposition of the total field using a fixed incident and unknown reflected field:

$$\mathrm{H} = \mathrm{H}_{\mathrm{inc}} + \mathrm{H}_{\mathrm{sc}} \quad \text{with} \quad \mathrm{H}_{\mathrm{inc}}(x,y) = e^{-ik_0(y-y_0)} \quad \text{and } \mathrm{H}_{\mathrm{sc}} \text{ which verifies radiation conditions at infinity.}$$

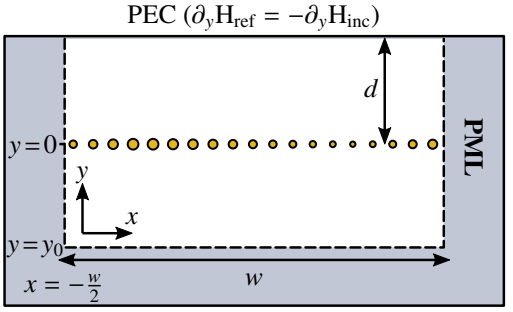

Fig. 13. Schematic representation and boundary conditions verified by the field H_{sc} in the open metasurfaces considered in section 4.2. The PML regions are in gray and terminated by PEC. The incident field $\mathrm{H}_{\mathrm{inc}}$ is null inside the PMLs.

This time, we will directly try to find the weak formulation associated with the reflected field H_{sc}. In addition, to limit the size of the simulation domain, Perfectly Matched Layers (PML) of length $\lambda_0/2$ will be used to emulate the radiation conditions as represented in fig. 13 and in which only the reflected field is defined ($\mathrm{H}_{\mathrm{inc}} = 0$). We denote by O the full simulation domain, O_{PML} the PML regions and $O_{\mathrm{inc}} = O \backslash O_{\mathrm{PML}}$.

To derive the weak formulation associated with H_{sc} in the open domain O, we follow the presentation of section 2.8. First, the reflected field in O_{inc} verifies $-\nabla \cdot (1/\varepsilon_r \nabla \mathrm{H}_{\mathrm{sc}}) - k_0^2 \mathrm{H}_{\mathrm{sc}} = \nabla \cdot (1/\varepsilon_r \nabla \mathrm{H}_{\mathrm{inc}}) + k_0^2 \mathrm{H}_{\mathrm{inc}}$.

Secondly, due to the presence of PMLs, the Helmholtz equations are modified in O_{PML} so that the reflected field is solution there of

$$-\nabla \cdot \left(\overline{\overline{\Lambda}} \mathrm{H}_{\mathrm{sc}} \right) - k_0^2 \sigma \mathrm{H}_{\mathrm{sc}} = 0$$

where σ and $\overline{\overline{\Lambda}}$ are PML-dependent parameters given by:

$$\sigma(x,y) = \sigma_x \sigma_y \quad \text{and} \quad \overline{\overline{\Lambda}}(x,y) = \begin{pmatrix} \sigma_y/\sigma_x & 0 \\ 0 & \sigma_x/\sigma_y \end{pmatrix},$$

with $\sigma_x(x)$ (resp. $\sigma_y(y)$) equal to $2\lambda_0(1-i)$ if $|x| > w/2$ (resp. if $y < y_0$) and 1 otherwise. From an integration by parts it follows that H_{sc} is solution for all test functions ϕ of:

$$a_{\mathrm{H}}^{\sigma,\varepsilon}(\mathrm{H}_{\mathrm{sc}}, \phi) = b_{\mathrm{H}}^{\sigma,\varepsilon}(\phi),$$

where the sesquilinear and linear forms are defined by:

$$a_{\mathrm{H}}^{\sigma,\varepsilon}(\mathrm{H}_{\mathrm{sc}},\phi) := \int_{O_{\mathrm{PML}}} \overline{\overline{\Lambda}}\nabla\mathrm{H}_{\mathrm{sc}}\cdot\nabla\phi^* - k_0^2\sigma\mathrm{H}_{\mathrm{sc}}\phi^*\,\mathrm{d}\boldsymbol{x} + \int_{O_{\mathrm{inc}}} \frac{1}{\varepsilon_r}\nabla\mathrm{H}_{\mathrm{sc}}\cdot\nabla\phi^* - k_0^2\mathrm{H}_{\mathrm{sc}}\phi^*\,\mathrm{d}\boldsymbol{x},$$
$$b_{\mathrm{H}}^{\sigma,\varepsilon}(\phi) := \int_{O_{\mathrm{inc}}} -\frac{1}{\varepsilon_r}\nabla\mathrm{H}_{\mathrm{inc}}\cdot\nabla\phi^* + k_0^2\mathrm{H}_{\mathrm{inc}}\phi^*\,\mathrm{d}\boldsymbol{x} + \int_{\partial O_{\mathrm{inc}}\setminus\{\boldsymbol{x},y=d\}} \mathbf{n}\cdot\nabla\mathrm{H}_{\mathrm{inc}}\phi^*\,\mathrm{d}\boldsymbol{x},$$

with $\mathbf{n}$ going outside of O_{inc}. Equivalently, the effective reflected field still noted by H_{sc} is given as the solution to:

$$a_{\mathrm{H}}^{\sigma}(\mathrm{H}_{\mathrm{sc}},\phi) + b_{\Gamma}(\mathrm{H}_{\mathrm{sc}},\phi) = b_{\Gamma}^{\sigma}(\phi),$$

where b_Γ was defined in eq. (32) while the other forms are given by:

$$a_{\mathrm{H}}^{\sigma}(\mathrm{H}_{\mathrm{sc}},\phi) := \int_{O_{\mathrm{PML}}} \overline{\overline{\Lambda}}\nabla\mathrm{H}_{\mathrm{sc}}\cdot\nabla\phi^* - k_0^2\sigma\mathrm{H}_{\mathrm{sc}}\phi^*\,\mathrm{d}\boldsymbol{x} + \int_{O_{\mathrm{inc}}} \nabla\mathrm{H}_{\mathrm{sc}}\cdot\nabla\phi^* - k_0^2\mathrm{H}_{\mathrm{sc}}\phi^*\,\mathrm{d}\boldsymbol{x},$$
$$b_{\Gamma}^{\sigma}(\phi) := \int_{O_{\mathrm{inc}}} -\nabla\mathrm{H}_{\mathrm{inc}}\cdot\nabla\phi^* + k_0^2\mathrm{H}_{\mathrm{inc}}\phi^*\,\mathrm{d}\boldsymbol{x} + \int_{\partial O_{\mathrm{inc}}\setminus\{\boldsymbol{x},y=d\}} \mathbf{n}\cdot\nabla\mathrm{H}_{\mathrm{inc}}\phi^*\,\mathrm{d}\boldsymbol{x} - b_{\Gamma}(\mathrm{H}_{\mathrm{inc}},\phi).$$

Note that using Huygens principle [32], it is not necessary to consider a large domain O_{inc} that contains the focal point $\boldsymbol{x}_0$; we can have $f_0 < y_0$. Indeed, using the Green function $G_{\mathbf{0}}(x,y) := \frac{1}{4i}H_0^{(2)}\left(k_0\sqrt{x^2+y^2}\right)$ of the Helmholtz equation where $H_0^{(2)}$ is the Hankel function of second order, the reflected field at any $Y < y_0$ can be found as:

$$\mathrm{H}_{\mathrm{sc}}(X,Y) = -2\int_{\Gamma_0} \mathrm{H}_{\mathrm{sc}}(x,y_0)\partial_y G_{\mathbf{0}}(x-X,y_0-Y)\,\mathrm{d}x.$$

4.2.2. Local phase-based design

The local phase change of a perfect lens is well known [33, Eq. (1)][34, Eq. (4)]. Following the explanation given in section 3.2, it can be obtained by considering that the reflected field must follow the Green's function of the Helmholtz equation centered at $\boldsymbol{x}_0$; a "perfect" lens is achieved if the reflected field below the metasurface is given by:

$$\mathrm{H}_{\mathrm{sc}}^{\star}(x,y) = \alpha H_0^{(2)}\left(k_0\sqrt{x^2+(f_0-y)^2}\right),$$

where α is a proportionality factor for the reflected wave amplitude (we remind that the LPM does not take into account the amplitude of the desired field and therefore it is not necessary to explicit the value of α). Asymptotically, when the focal distance f_0 is at least a few wavelength below Γ, we can use the formula $H_0^{(2)}(r) \sim \sqrt{2/(\pi r)}e^{ir}$ which is valid for large values of r. This lead to an expected phase of

$$\phi_{\mathrm{lens}}^{\star}(x) = k_0\sqrt{x^2+(f_0-y_0)^2} \quad \text{modulo } 2\pi$$

on the fictituous plane Γ_0 at $y = y_0$. Note that the important part of the lens is the one near its center at $x = 0$ and we have therefore moved ϕ_{lens} to zero at $x = 0$ since a phase change of zero is well-obtained with our meta-atoms (see fig. 6 (b) for a radius $\simeq 0.1 s_\eta$).

4.2.3. Sensitivity of the energy density

As in the test case of the deflector, we will start by defining a figure of merit to measure the performance of the lens. Since the goal of such a structure is to make the reflected field focus at the focal position $\boldsymbol{x}_0$, this amounts to maximize the function

$$F_{\mathrm{lens}}(\rho) := |\mathrm{H}_{\mathrm{sc}}(\boldsymbol{x}_0)|^2. \tag{37}$$

As before, the derivation is performed in Appendix C.2 and the result is summarized below. The gradient associated with eq. (37) is given by:

$$G_{\mathrm{lens}}(\rho) = 2\mathcal{R}e\left[\mathrm{H}_{\mathrm{sc}}(\boldsymbol{x}_0)^*\left(\frac{(\chi_{ee}^{xx})'(\rho)}{(\chi_{ee}^{xx})^2(\rho)}[\![\mathrm{H}_{\mathrm{sc}}]\!][\![p]\!] + (\chi_{ee}^{yy})'(\rho)\partial_x\{\mathrm{H}_{\mathrm{sc}}\}\partial_x\{p\}\right)\right], \tag{38}$$

where the adjoint p is solution to $a_{\mathrm{H}}^{\sigma}(p,\phi) + b_{\Gamma}(p,\phi) = \phi(\boldsymbol{x}_0)^*$. In other words, *the adjoint p is the field obtained with a point source centered at the focal point* (which is equivalent to the presence of a magnetic point dipole of moment $\mathbf{m} = \mathbf{u}_z$ at $\boldsymbol{x}_0$).

4.2.4. Classical lenses

We now consider a metasurface of size $w = 25\lambda_0$ (since $\eta = 1/20$ this implies that the metasurface is composed of 500 meta-atoms) with a normal incident plane wave. We propose to optimize the metalens for different values of f_0 varying between $2.5\lambda_0$ and $20\lambda_0$ which corresponds to a numerical aperture NA$= (w/2)/((w/2)^2 + f_0^2)^{1/2}$ between 0.53 and 0.98. The results are summarized in fig. 14. Each optimization takes less than 10 minutes for the 250 iterations of the optimization algorithm with the effective field, while the meshing and simulation of the resulting design takes a few minutes for the direct field.

f_0/λ_0	2.5	5	10	15	20
LP-based design	0.15	0.24	0.33	0.41	0.45
H-based design	0.31	0.44	0.55	0.56	0.55
Improvement	+110%	+86%	+65%	+36%	+21%

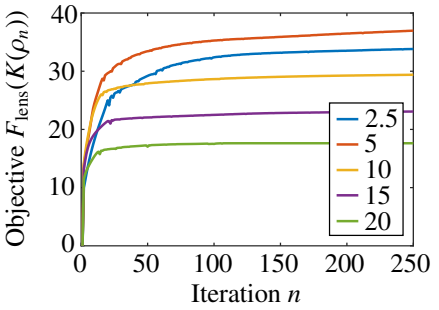

Table 2. Comparison of the lenses (focusing efficiency calculated with direct simulations and eq. (39)) obtained using either the LPM or the optimized designs after 250 iterations.

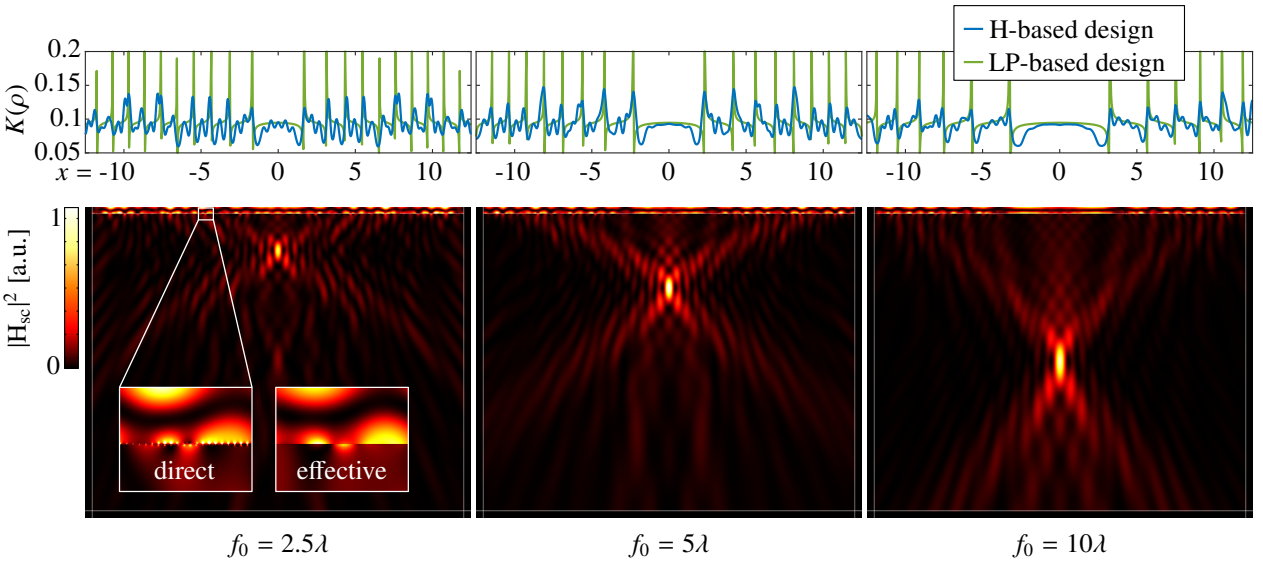

Fig. 14. Reflected energy density (same amplitude in the colorbars) for the optimized metalenses with focal distances varying between $f_0 = 2.5\lambda_0$ and $f_0 = 10\lambda_0$ using direct simulations.

The objective function $F_{\mathrm{lens}}(\rho)$ of eq. (37) has been considered for the lens optimization, but in practice, a more commonly commented figure of merit is obtained by examining the percentage of power sent to the lens that is reflected near the focal point[6]. Precisely, using the y component of the Poynting vector, we define the focusing

[6]This objective function was not considered as its derivative is more convoluted due to the FWHM that has to be computed at each iteration.

efficiency following [35, Section 4] as:

$$\mathcal{P} := -\frac{\mathcal{P}_{\mathcal{F}_{\text{FWHM}}}(\mathrm{H_{sc}})}{\mathcal{P}_{\Gamma_0}(\mathrm{H_{inc}})} \quad \text{where for all set } O \text{ and field } A, \quad \mathcal{P}_O(A) = \int_O \mathcal{R}e\left[A^* \partial_y A / i\right] \, \mathrm{d}x, \tag{39}$$

with $\mathcal{F}_{\text{FWHM}} = (-3h/2, 3h/2) \times \{f_0\}$ and h is the Full Width at Half Maxima (FWHM) on the focal plane $\mathcal{F}_0 = \{\boldsymbol{x}, y = f_0\}$. If x_- and x_+ are the biggest and smallest x such that $|\mathrm{H_{sc}}(x_\pm, f_0)|^2 < 1/2|\mathrm{H_{sc}}(\boldsymbol{x}_0)|^2$ and $x_- < 0, x_+ > 0$ then we define $h := x_+ - x_-$. Once again, we compare in table 2 the designs obtained with the LPM and the optimization algorithm.

As in the case of the deflector, we find that the increase in performance obtained with the optimization method is more important when the LP-based designs involve a lot of steep variations, that is, for a small focal distance (i.e., a high numerical aperture).

4.2.5. Coating

In this last example, we consider a curved metasurface (such a system could be considered for instance in cloaking applications where a shape is coated with a microstructure [34]) for which the GSTC are changed into locally curved coordinates by changing the ∂_y into normal derivatives and the ∂_x by tangential ones (see [36] for more details about the FEM implementation). The interface Γ is defined via:

$$\Gamma_{1/4} := \{4(-5t^4 + 10t^3 - 6t^2 + 1, -5t^4 + 10t^3 - 6t^2 + 2t), t \in [0, 1]\},$$

which is then symmetrized around $x = 0$ and $y = 0$ to obtain the four parts of Γ[7].

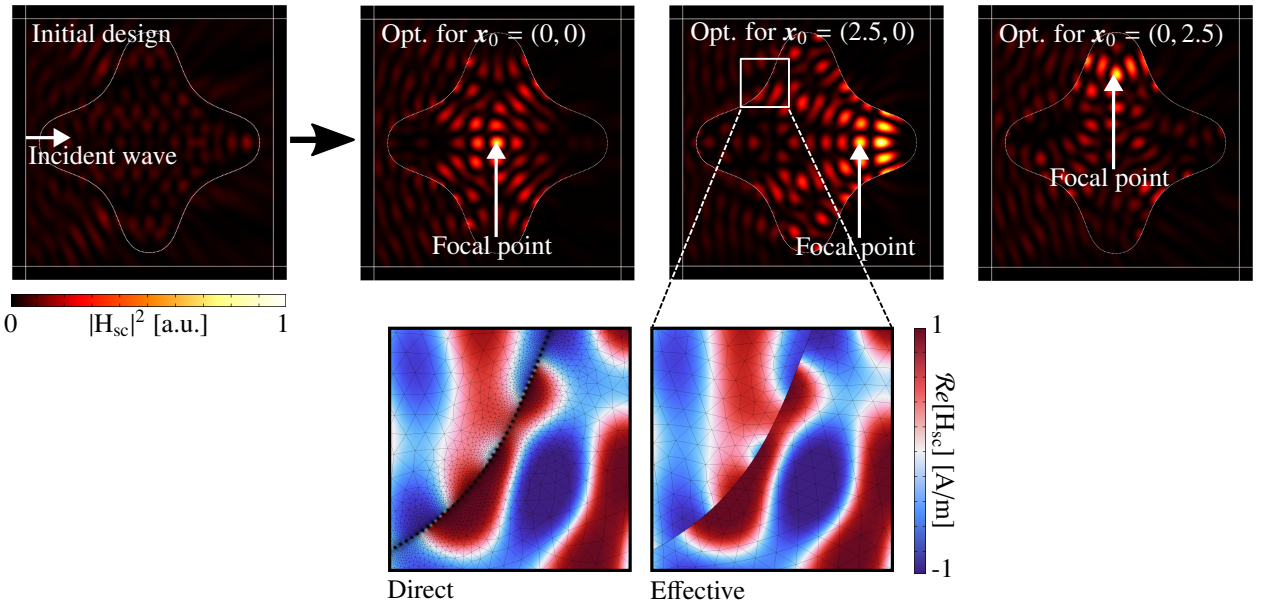

Fig. 15. Optimized designs for three curved metalenses with different focal points x_0 starting with $\rho_0(x) = r_{\text{min}}$ and an incident plane wave coming from the left side. The fields at the bottom show the meshes used in the direct and effective simulations.

Our goal is to design the meta-atoms distributions such that the curved metasurface act as a lens when an incident plane wave is sent from the left of the domain. This example is interesting as complex interactions happens between the meta-atoms inside the region surrounded by the metasurface which are adequately taken into account in the effective finite element simulations as the homogenized model is valid for any angle of incidence. The result of our optimizations after 500 iterations are summarized in fig. 15 and shows that the algorithm is able to optimize the considered figure of merit even in cases where the waves can interact many times with the metasurface.

[7] Note that Γ is also scaled a little bit such that its length ends in a multiple of the period $\eta = 1/20$ which results in 483 meta-atoms.

5. Conclusion

In conclusion, we have presented a homogenized model for plasmonic metasurfaces that works even in the presence of quasi-periodic resonant meta-atoms. This model, once implemented in a finite element software, provide a way to ease the calculation of such metasurfaces. Using these fast simulations which rely on a smooth distribution of geometrical parameters, we have shown that it is possible to optimize metasurfaces and to obtain performances superior to those obtained with the local phase matching method while also being adaptable to other contexts. At first glance, however, this result was not necessarily predictable. Indeed, as we have seen in section 2, the GSTCs are based on a local periodicity approximation which appears in the solution of the static elementary problems, just like the LPM method of section 3.2 which is based on the simulation of meta-atoms by the Helmholtz equation with periodic boundary conditions. However, only the homogenization theory provides an accurate model up to order 2 (see for example [37]). The application of our methodology to three-dimensional domains should be even more interesting as it will further reduce the number of degrees of freedom to be solved during the FEM simulations. Although the examples considered in this study rely on plasmonic resonances, other resonance phenomena could be considered, including Mie resonances [38] or split-ring resonators [39, 40]. It should also be pointed that in this study, we have only relied on geometrically parameterized meta-atoms, while it could also be possible to consider the simultaneous shape (or topology) optimization of each individual cell [41, 42].

Acknowledgments:

A.M. acknowledge support from LABEX WIFI (Laboratory of Excellence within the French Program "Investments for the Future") under references ANR-10-LABX-24 and ANR-10-IDEX-0001-02 PSL*. K.P. acknowledges support from the Agence de l'Innovation de Défense (AID) from the Direction Générale de l'Armement (DGA), under grant no. 2019 65 0070 and the Agence Nationale de la Recherche under grant ANR-19-CE08-0006.

Appendix A. Phase change induced by plasmonic meta-atoms in transmission

We have decided in this paper to work only with metasurfaces in reflection, a choice that we justify here. In the case of a periodic metasurface in transmission with normal-incident plane waves, the field above and below the metasurface can be decomposed into

$$\mathrm{H}(x, y < 0) = e^{-ik_0(y-y_0)} + Re^{-i(\phi_R - k_0(y-y_0))} \quad \text{and} \quad \mathrm{H}(x, y > 0) = Te^{-i(\phi_T + k_0(y-y_0))}.$$

Using the GSTCs of eqs. (20) and (21), we can show that the transmission is given by:

$$Te^{-i\phi_T} = \frac{4 - 2ik_0\chi_{ee}^{xx}}{4 + k_0^2(\chi_{ee}^{xx})^2}. \tag{A.1}$$

For lossless materials (i.e. real-valued susceptibilities), the right-hand side of eq. (A.1) always has a positive real value. This implies that $\phi_T \in (-\pi/2, \pi/2)$, i.e., a (deeply subwavelength) lossless plasmonic and two-dimensional meta-atom in transmission cannot induce a phase change greater than π. This prevents the use of the local phase change method described in section 3.2 to control the transmitted field. Our optimization method could still be used but we have preferred to consider test cases where the two methods could be legitimately compared.

Appendix B. Phase change induced by plasmonic meta-atoms in reflection

In the case of a reflective metasurface placed at a distance d from a perfect conductor as defined in section 3.1, the field is decomposed into:

$$\mathrm{H}(x, y < 0) = e^{-ik_0(y-y_0)} + Re^{-i(\phi_R - k_0(y-y_0))} \quad \text{and} \quad \mathrm{H}(x, y \in (0, d)) = T_1 e^{-i(\phi_{T_1} + k_0(y-y_0))} + R_1 e^{-i(\phi_{R_1} - k_0(y-y_0))}.$$

Using the GSTCs of eqs. (20) and (21), we can show that the reflection is given by:

$$Re^{-i\phi_R} = \frac{k_0\chi_{ee}^{xx}\sin(k_0 d) - e^{-ik_0 d}}{k_0\chi_{ee}^{xx}\sin(k_0 d) - e^{ik_0 d}} \quad \text{and in particular that} \quad \phi_R = -2\arctan\left(\frac{\sin(k_0 d)}{k_0\chi_{ee}^{xx}\sin(k_0 d) - \cos(k_0 d)}\right). \tag{B.1}$$

If the distance d is such that $k_0 d = \pi/2$ modulo 2π then whatever the meta-atoms composing the plasmonic metasurface, they have no influence on the reflected field. In all the other cases, when χ_{ee}^{xx} cover the whole range $(-\infty, +\infty)$ (which is only possible around a resonance) then so do the phase in the interval $(-\pi, \pi)$. In particular, the phase exhibit rapid changes when $k_0 \chi_{ee}^{xx} \sin(k_0 d) - \cos(k_0 d) = \pm 0$, that is for a susceptibility $\chi_{ee}^{xx} = k_0^{-1} \cot(k_0 d)$. Since χ_{ee}^{xx} is always different than 0 (as can be seen in fig. 9), considering a distance d such that $k_0 d = \pi$ modulo 2π ($d = \lambda_0/2$) is not the best choice as in this case the rapid change in the phase is never crossed since it happen for $\chi_{ee}^{xx} = 0$.

Since eq. (B.1) is valid for all distances d, we have computed R and ϕ_R for different choices of d as in fig. B.16 and set d to 0.45λ as it allows to almost obtain the 2π phase change required by the LPM. The minimum and maximum relative radius were chosen so that only one resonance is covered.

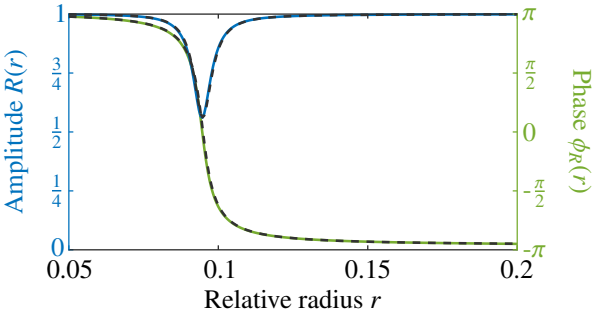

Fig. B.16. Amplitude and phase of the reflected field for the periodic meta-atoms of fig. 5 computed using the effective transition conditions and the analytic reflection coefficients given by eq. (B.1). For reference, the dashed black lines are the curves obtained through direct simulation of the Helmholtz equation (same as fig. 5 (right)).

It is interesting to note the very good agreement in fig. 5 between the effective model and the direct simulations. The average error is 0.15 % in amplitude and 0.59° in phase. Near the resonance at $\sim r = 0.1$, the maximum error is 2.18 % in amplitude and 9.59° in phase.

Appendix C. Derivation of the gradients

This appendix is dedicated to the derivation of the gradients $G(\rho)$ of eqs. (34) and (37) as defined in eq. (25).

Appendix C.1. Deflectors

Introducing $\mathring{\mathrm{H}}$ (resp. $\mathring{\mathbf{R}}^{\mathrm{H}}$) the derivative of H (resp. $\mathbf{R}^{\mathrm{H}}$) w.r.t. ρ along $\tilde{\rho}$, a formal derivation of the objective function eq. (34) gives that:

$$F_{\text{deflector}}(\rho)'(\tilde{\rho}) = 2\mathcal{R}e\Big[(\mathrm{R}_N^{\mathrm{H}})^* \mathring{\mathrm{R}}_N^{\mathrm{H}}\Big]. \tag{C.1}$$

The derivation of eq. (31) shows that $(\mathring{\mathrm{H}}, \mathring{\mathbf{R}}^{\mathrm{H}})$ are solutions to

$$a_{\mathrm{H}}(\mathring{\mathrm{H}}, \phi) + a_{\mathrm{R}}(\mathring{\mathbf{R}}^{\mathrm{H}}, \mathbf{R}^{\phi}) + b_{\Gamma}(\mathring{\mathrm{H}}, \phi) = -b'_{\Gamma}(\mathrm{H}, \phi) \quad \text{with the constraint} \quad \mathring{\mathrm{H}}(x, y_0) = \sum_n \mathring{\mathrm{R}}_n^{\mathrm{H}} \mathrm{H}_n^{\downarrow}, \tag{C.2}$$

where

$$b'_{\Gamma}(\mathrm{H}, \phi) = -\int_{\Gamma} \left[\frac{(\chi_{ee}^{xx})'(\rho)}{(\chi_{ee}^{xx})^2(\rho)} [\![\mathrm{H}]\!] [\![\phi^*]\!] + \left(\chi_{ee}^{yy}\right)'(\rho) \partial_x \{\mathrm{H}\} \partial_x \{\phi^*\} \right] \tilde{\rho} \, \mathrm{d}x. \tag{C.3}$$

Note that following the discussion in section 3.3, we consider that χ_{ee}^{xx} and χ_{ee}^{yy} are known functions and that their derivatives can be obtained, for example, through finite differences[8] of fig. 9. It would be possible to solve eq. (C.2)

[8] Note that because of the discontinuity of χ_{ee}^{xx}, it is more stable to compute $(1/\chi_{ee}^{xx})'(\rho)$ directly (which is equal to $-(\chi_{ee}^{xx})'(\rho)/(\chi_{ee}^{xx})^2(\rho)$) using finite differences.

directly for any $\tilde{\rho}$ to find $\mathring{\mathrm{R}}_N^{\mathrm{H}}$ but this won't give us an indication on which perturbation should be considered in order to improve $F(\rho)$. To simplify eq. (C.1), we introduce an "adjoint" state $(p, \mathbf{R}^p)$ solution to

$$a_{\mathrm{H}}(p,\phi) + a_{\mathrm{R}}(\mathbf{R}^p,\mathbf{R}^\phi) + b_\Gamma(p,\phi) = l^{-N}(\mathbf{R}^\phi) \quad \text{with the constraint} \quad p(x,y_0) = \mathrm{H}^{\uparrow}_{-N} + \sum_n \mathrm{R}^p_n \mathrm{H}^{\downarrow}_n. \tag{C.4}$$

In other words, *the adjoint p is the field obtained when injecting a plane wave in the $-N$-th order of reflection of interest.* Manipulations of the fields constraints can be used to show that both $(\phi, \mathbf{R}^\phi) = (p^*, \mathbf{R}^{p*} + (\delta_{n,N})_n)$ and $(\phi, \mathbf{R}^\phi) = (\mathring{\mathrm{H}}^*, \mathring{\mathbf{R}}^{\mathrm{H}*})$ where $\mathrm{R}^{p*}_n = (\mathrm{R}^p_{-n})^*$ and $\mathring{\mathrm{R}}^{\mathrm{H}*}_n = (\mathring{\mathrm{R}}^{\mathrm{H}}_{-n})^*$ verifies the constraint of eq. (29). Injecting these values in eqs. (C.2) and (C.4) we find that:

$$\begin{aligned} a_{\mathrm{H}}(\mathring{\mathrm{H}}, p^*) + a_{\mathrm{R}}(\mathring{\mathbf{R}}^{\mathrm{H}}, \mathbf{R}^{p*}) + a_{\mathrm{R}}(\mathring{\mathbf{R}}^{\mathrm{H}}, (\delta_{n,N})_n) + b(\mathring{\mathrm{H}}, p^*) &= -b'(\mathrm{H}, p^*), \\ a_{\mathrm{H}}(p, \mathring{\mathrm{H}}^*) + a_{\mathrm{R}}(\mathbf{R}^p, \mathring{\mathbf{R}}^{\mathrm{H}*}) + b(p, \mathring{\mathrm{H}}^*) &= l^{-N}(\mathring{\mathbf{R}}^{\mathrm{H}*}). \end{aligned}$$

Or, we have:

$$a_{\mathrm{R}}(\mathring{\mathbf{R}}^{\mathrm{H}}, \mathbf{R}^{p*}) = iw \sum_n k_{y,n} |A_n|^2 \mathring{\mathrm{R}}^{\mathrm{H}}_n \mathrm{R}^p_{-n}, \quad a_{\mathrm{R}}(\mathbf{R}^p, \mathring{\mathbf{R}}^{\mathrm{H}*}) = iw \sum_n k_{y,n} |A_n|^2 \mathrm{R}^p_n \mathring{\mathrm{R}}^{\mathrm{H}}_{-n},$$

and by equality of $A_n, k_{y,n}$ with $A_{-n}, k_{y,-n}$, both sesquilinear forms are equals. Similarly for a_{H} and b which lead to:

$$l^{-N}(\mathring{\mathbf{R}}^{\mathrm{H}*}) = -b'(\mathrm{H}, p^*) - a_{\mathrm{R}}(\mathring{\mathbf{R}}^{\mathrm{H}}, \delta_{n,N}) \quad \Leftrightarrow \quad iwk_{y,N}|A_N|^2 \mathring{\mathrm{R}}^{\mathrm{H}}_N = -b'(\mathrm{H}, p^*) - iwk_{y,N}|A_N|^2 \mathring{\mathrm{R}}^{\mathrm{H}}_N,$$

that is:

$$\mathring{\mathrm{R}}^{\mathrm{H}}_N = -\frac{b'(\mathrm{H}, p^*)}{2iwk_{y,N}|A_N|^2}.$$

Now from from eq. (C.1) we get:

$$F_{\text{deflector}}(\rho)'(\tilde{\rho}) = -2\mathcal{R}e\left[(\mathrm{R}^{\mathrm{H}}_N)^* \frac{b'(\mathrm{H}, p^*)}{2iwk_{y,N}|A_N|^2} \right].$$

From the definition of $G_{\text{deflector}}(\rho)$ in eq. (25) as $F_{\text{deflector}}(\rho)'(\tilde{\rho}) = \int_\Gamma G_{\text{deflector}}(\rho)\tilde{\rho}\, \mathrm{d}x$ and eq. (C.3) we find the result of eq. (35).

Appendix C.2. Lenses

A formal derivation of the objective function eq. (37) lead to:

$$F_{\text{lens}}(\rho)'(\tilde{\rho}) = 2\mathcal{R}e\Big[\mathrm{H}_{\mathrm{sc}}(\boldsymbol{x}_0)^* \mathring{\mathrm{H}}_{\mathrm{sc}}(\boldsymbol{x}_0) \Big], \tag{C.5}$$

where $\mathring{\mathrm{H}}_{\mathrm{sc}}$ is solution to (remember that b'_Γ is defined in eq. (C.3)):

$$a^\sigma_{\mathrm{H}}(\mathring{\mathrm{H}}_{\mathrm{sc}}, \phi) + b_\Gamma(\mathring{\mathrm{H}}_{\mathrm{sc}}, \phi) = -b'_\Gamma(\mathrm{H}_{\mathrm{sc}}, \phi). \tag{C.6}$$

This time the adjoint is defined as the field p solution to:

$$a^\sigma_{\mathrm{H}}(p, \phi) + b_\Gamma(p, \phi) = \phi(\boldsymbol{x}_0)^*. \tag{C.7}$$

Taking $\phi = p^*$ in eq. (C.6) and $\phi = \mathring{\mathrm{H}}^*_{\mathrm{sc}}$ in eq. (C.7) gives that:

$$\begin{aligned} a^\sigma_{\mathrm{H}}(\mathring{\mathrm{H}}_{\mathrm{sc}}, p^*) + b_\Gamma(\mathring{\mathrm{H}}_{\mathrm{sc}}, p^*) &= -b'_\Gamma(\mathrm{H}, p^*), \\ a^\sigma_{\mathrm{H}}(p, \mathring{\mathrm{H}}^*_{\mathrm{sc}}) + b_\Gamma(p, \mathring{\mathrm{H}}^*_{\mathrm{sc}}) &= \mathring{\mathrm{H}}_{\mathrm{sc}}(\boldsymbol{x}_0), \end{aligned}$$

which lead to $\mathring{\mathrm{H}}_{\mathrm{sc}}(\boldsymbol{x}_0) = -b'_\Gamma(\mathrm{H}, p^*)$. Injecting this expression in eq. (C.5) with $F_{\text{lens}}(\rho)'(\tilde{\rho}) = \int_\Gamma G_{\text{lens}}(\rho)\tilde{\rho}\, \mathrm{d}x$ result in eq. (38).

References

[1] S. B. Glybovski, S. A. Tretyakov, P. A. Belov, Y. S. Kivshar, C. R. Simovski, Metasurfaces: From microwaves to visible, Physics reports 634 (2016) 1–72.

[2] C. L. Holloway, E. F. Kuester, A homogenization technique for obtaining generalized sheet-transition conditions for a metafilm embedded in a magnetodielectric interface, IEEE Transactions on Antennas and Propagation 64 (2016) 4671–4686.

[3] N. Yu, P. Genevet, M. A. Kats, F. Aieta, J.-P. Tetienne, F. Capasso, Z. Gaburro, Light propagation with phase discontinuities: generalized laws of reflection and refraction, science 334 (2011) 333–337.

[4] F. Ding, A. Pors, S. I. Bozhevolnyi, Gradient metasurfaces: a review of fundamentals and applications, Reports on Progress in Physics 81 (2017) 026401.

[5] N. Yu, P. Genevet, F. Aieta, M. A. Kats, R. Blanchard, G. Aoust, J.-P. Tetienne, Z. Gaburro, F. Capasso, Flat optics: controlling wavefronts with optical antenna metasurfaces, IEEE Journal of Selected Topics in Quantum Electronics 19 (2013) 4700423–4700423.

[6] L. Hsu, T. Lepetit, B. Kanté, Extremely thin dielectric metasurface for carpet cloaking, arXiv preprint arXiv:1503.08486 (2015).

[7] N. M. Estakhri, A. Alù, Ultra-thin unidirectional carpet cloak and wavefront reconstruction with graded metasurfaces, IEEE Antennas and Wireless Propagation Letters 13 (2014) 1775–1778.

[8] H. Esfahlani, S. Karkar, H. Lissek, J. R. Mosig, Acoustic carpet cloak based on an ultrathin metasurface, Physical Review B 94 (2016) 014302.

[9] C. Pfeiffer, A. Grbic, Metamaterial huygens' surfaces: tailoring wave fronts with reflectionless sheets, Physical review letters 110 (2013) 197401.

[10] G. Allaire, Homogenization and two-scale convergence, SIAM Journal on Mathematical Analysis 23 (1992) 1482–1518.

[11] C. L. Holloway, E. F. Kuester, A. Dienstfrey, Characterizing metasurfaces/metafilms: The connection between surface susceptibilities and effective material properties, IEEE Antennas and Wireless Propagation Letters 10 (2011) 1507–1511.

[12] B. Delourme, E. Lunéville, J.-J. Marigo, A. Maurel, J.-F. Mercier, K. Pham, A stable, unified model for resonant faraday cages, Proceedings of the Royal Society A 477 (2021) 20200668.

[13] N. Lebbe, K. Pham, A. Maurel, Stable gstc formulation for maxwell's equations, IEEE Transactions on Antennas and Propagation (2022).

[14] B. Delourme, H. Haddar, P. Joly, Approximate models for wave propagation across thin periodic interfaces, Journal de mathématiques pures et appliquées 98 (2012) 28–71.

[15] A. Maurel, K. Pham, J.-J. Marigo, Homogenization of thin 3d periodic structures in the time domain–effective boundary and jump conditions, Fundamentals and Applications of Acoustic Metamaterials: From Seismic to Radio Frequency 1 (2019) 73–105.

[16] E. Rohan, V. Lukeš, Homogenization of the acoustic transmission through a perforated layer, Journal of Computational and Applied Mathematics 234 (2010) 1876–1885.

[17] K. Pham, A. Maurel, J.-J. Marigo, Two scale homogenization of a row of locally resonant inclusions-the case of anti-plane shear waves, Journal of the Mechanics and Physics of Solids 106 (2017) 80–94.

[18] K. Pham, A. Maurel, J.-J. Marigo, Revisiting imperfect interface laws for two-dimensional elastodynamics, Proceedings of the Royal Society A 477 (2021) 20200519.

[19] L.-P. Euvé, K. Pham, P. Petitjeans, V. Pagneux, A. Maurel, Time domain modelling of a helmholtz resonator analogue for water waves, Journal of Fluid Mechanics 920 (2021) A22.

[20] K. Pham, J.-F. Mercier, D. Fuster, J.-J. Marigo, A. Maurel, Scattering of acoustic waves by a nonlinear resonant bubbly screen, Journal of Fluid Mechanics 906 (2021) A19.

[21] G. Allaire, E. Bonnetier, G. Francfort, F. Jouve, Shape optimization by the homogenization method, Numerische Mathematik 76 (1997) 27–68.

[22] K. Pham, N. Lebbe, A. Maurel, Diffraction grating with varying slit width: Quasi-periodic homogenization and its numerical implementation, Journal of Computational Physics 473 (2023) 111727.

[23] N. Lebbe, A. Maurel, K. Pham, Homogenized transition conditions for plasmonic metasurfaces, Physical Review B 107 (2023) 085124.

[24] Y. Noguchi, T. Yamada, Topology optimization of acoustic metasurfaces by using a two-scale homogenization method, Applied Mathematical Modelling 98 (2021) 465–497.

[25] K. Achouri, M. A. Salem, C. Caloz, General metasurface synthesis based on susceptibility tensors, IEEE Transactions on Antennas and Propagation 63 (2015) 2977–2991.

[26] L. Hsu, M. Dupré, A. Ndao, J. Yellowhair, B. Kanté, Local phase method for designing and optimizing metasurface devices, Optics express 25 (2017) 24974–24982.

[27] M. P. Bendsøe, N. Kikuchi, Generating optimal topologies in structural design using a homogenization method, Computer methods in applied mechanics and engineering 71 (1988) 197–224.

[28] J. P. Groen, O. Sigmund, Homogenization-based topology optimization for high-resolution manufacturable microstructures, International Journal for Numerical Methods in Engineering 113 (2018) 1148–1163.

[29] B. S. Lazarov, O. Sigmund, Filters in topology optimization based on helmholtz-type differential equations, International Journal for Numerical Methods in Engineering 86 (2011) 765–781.

[30] COMSOL AB, Stockholm, Sweden, Wave Optics Module User's Guide, COMSOL Multiphysics®, 2022. URL: www.comsol.com.

[31] B. Vial, Y. Hao, Open-source computational photonics with auto differentiable topology optimization, Mathematics 10 (2022) 3912.

[32] J.-M. Jin, The finite element method in electromagnetics, John Wiley & Sons, 2015.

[33] M. Pan, Y. Fu, M. Zheng, H. Chen, Y. Zang, H. Duan, Q. Li, M. Qiu, Y. Hu, Dielectric metalens for miniaturized imaging systems: progress and challenges, Light: Science & Applications 11 (2022) 195.

[34] X.-P. Wang, L.-L. Wan, T.-N. Chen, A.-L. Song, X.-W. Du, Broadband reflected wavefronts manipulation using structured phase gradient metasurfaces, AIP Advances 6 (2016) 065320.

[35] Z.-P. Zhuang, R. Chen, Z.-B. Fan, X.-N. Pang, J.-W. Dong, High focusing efficiency in subdiffraction focusing metalens, Nanophotonics 8 (2019) 1279–1289.

[36] N. Lebbe, S. Lanteri, S. Y. Golla, P. Genevet, Susceptibility synthesis of arbitrary shaped metasurfaces, Physical Review B 106 (2022) 035110.

[37] B. Delourme, H. Haddar, P. Joly, On the well-posedness, stability and accuracy of an asymptotic model for thin periodic interfaces in electromagnetic scattering problems, Mathematical Models and Methods in Applied Sciences 23 (2013) 2433–2464.
[38] G. Bouchitté, C. Bourel, D. Felbacq, Homogenization of the 3d maxwell system near resonances and artificial magnetism, Comptes Rendus Mathematique 347 (2009) 571–576.
[39] M. Farhat, S. Guenneau, S. Enoch, A. Movchan, Negative refraction, surface modes, and superlensing effect via homogenization near resonances for a finite array of split-ring resonators, Physical Review E 80 (2009) 046309.
[40] G. Bouchitté, B. Schweizer, Homogenization of maxwell's equations in a split ring geometry, Multiscale Modeling & Simulation 8 (2010) 717–750.
[41] Y. Noguchi, T. Yamada, Level set-based topology optimization for graded acoustic metasurfaces using two-scale homogenization, Finite Elements in Analysis and Design 196 (2021) 103606.
[42] B. Ahn, H. Lee, J. S. Lee, Y. Y. Kim, Topology optimization of metasurfaces for anomalous reflection of longitudinal elastic waves, Computer Methods in Applied Mechanics and Engineering 357 (2019) 112582.